THESIS FOR THE DEGREE OF DOCTOR OF PHILOSOPHY

Microstructure and Properties of Additively Manufactured Tool Steels for Hot Stamping

MIWEN YUAN

Department of Industrial and Materials Science

CHALMERS UNIVERSITY OF TECHNOLOGY

Gothenburg, Sweden 2023

Microstructure and Properties of Additively Manufactured Tool Steels for Hot Stamping

MIWEN YUAN

ISBN: 978-91-7905-786-2

© MIWEN YUAN, 2023.

Doktorsavhandlingar vid Chalmers tekniska högskola

Ny serie nr 5252

ISSN0346-718X

Department of Industrial and Materials Science
Chalmers University of Technology
SE-412 96 Gothenburg
Sweden Telephone + 46 (0)31-772 1000

Chalmers digitaltryck

Gothenburg, Sweden 2023

Microstructure and Properties of Additively Manufactured Tool Steels for Hot Stamping

Miwen Yuan
Department of Industrial and Materials Science
Chalmers University of Technology

Abstract:

Hot work tool steels are commonly used to produce dies for hot stamping, where the steels are exposed to cyclic thermal and mechanical loads. There is a constant demand to improve the lifetime of the dies. Additive manufacturing (AM) provides new solutions for tool design. For example, laser beam powder bed fusion (L-PBF) can print die with complex cooling channels, which can improve cooling efficiency and extend mould life. Directed energy deposition (DED) can easily do a hard facing for the tool surface and refurbish a worn die. This thesis evaluated the microstructure and properties of hot stamping tool steel fabricated by both L-PBF and DED techniques. The softening resistance was also assessed at elevated temperatures.

Before addressing the properties of AM tool steels, a case study was performed on the worn surface of a hot stamping insert die. Galling was observed, which was a result of accumulated layers transferred from the steel workpieces to the die. Material softening of the die was detected in the sublayer of ~ 200 μm. It is the softening of the die material that promotes galling. Galling together with the spalling of the white layer are supposed to be the primary wear mechanisms for the tool.

A modified H13 (M-H13) hot work tool steel was fabricated by L-PBF. The effect of two types of post-processing, direct tempering from as-built condition (DT) and conventional quenching followed by tempering (QT), on the microstructure and mechanical properties was evaluated. The softening resistance at elevated temperatures was investigated. Its correlation with the microstructure was also focused on. The evolution of carbides was discussed based on the microanalysis results and the JMatPro simulation.

Three different types of tool steels, Vanadias 4 Extra (V4E), a high-boron steel (HBS) and a newly developed maraging steel (NMS), were cladded on a hot work tool steel by means of DED for hard-facing purpose. For all tool steels, a near-dense cladded zone was obtained except V4E. Defects, including pores and cracks, were found in the deposited zone of V4E, the number of which increased with the building height or number of layers deposited. The factors that contribute to the formation of pores and cracks were identified.

After being tempered, the cladded tool steels were exposed at high temperatures to assess the softening resistance in terms of hardness. The abrasive wear resistance of the tempered and softened tool steels manufactured by DED was also evaluated at room temperature. A comparison with conventional counterparts on softening resistance and wear resistance was made. The microstructural evolution as a function of temperature and time was characterized and the precipitates were identified. Numerical simulations were applied to NMS to analyze the coarsening behavior of the precipitate and its influence on the mechanical property. The wear mechanism was discussed, and the governing factors were proposed.

Keywords: Tool Steels, Additive Manufacturing, Hot stamping, Softening Resistance, Wear.

Preface

The work presented in this doctoral thesis was conducted at the Department of Industrial and Materials Science at Chalmers University of Technology between February 2019 and January 2023. Research has been carried out under the supervision of Professor Yu Cao and the examination of Professor Lars Nyborg. The thesis has also been co-supervised by Professor Libin Liu and Dr Seshendra Karamchedu.

List of Appended Papers:

1. **A Case Study for a Worn Tool Steel in the Hot Stamping Process**
   M. Yuan, S. Karamchedu, Y. Fan, L. Liu, L. Nyborg, Y. Cao
   Journal of Materials Research and Technology 22 (2023):1065-1075.
   DOI: 10.1016/j.jmrt.2022.12.006
2. **Characteristics of a modified H13 hot-work tool steel fabricated by means of laser beam powder bed fusion**
   M. Yuan, Y. Cao, S. Karamchedu, S. Hosseini, Y. Yao, J. Berglund, L. Liu, L. Nyborg
   Materials Science and Engineering: A 831 (2022): 142322.
   DOI: 10.1016/j.msea.2021.142322
3. **Study of defects in directed energy deposited Vanadis 4 Extra tool steel**
   M. Yuan, S. Karamchedu, Y. Fan, L. Liu, L. Nyborg, Y. Cao
   Journal of Manufacturing Processes 76 (2022): 419-427.
   DOI: 10.1016/j.jmapro.2022.02.014
4. **Time and temperature dependent softening of a novel maraging steel fabricated by laser metal deposition**
   M. Yuan, L. Nyborg, C. Oikonomou, Y. Fan, L. Liu, Y. Cao
   Materials & Design 224 (2022): 111393.
   DOI: 10.1016/j.matdes.2022.111393
5. **Softening behavior of a cold work steel and high-boron tool steel fabricated by directed energy deposition**
   M. Yuan, L. Nyborg, C. Oikonomou, S. Karamchedu, Y. Fan, L. Liu, Y. Cao
   Manuscript
6. **Comparison of Softening Behavior and Abrasive Wear Resistance between Conventionally and Additively Manufactured Tool Steels**
   M. Yuan, L. Nyborg, C. Oikonomou, Y. Fan, L. Liu, J. Ye, Y. Cao
   Manuscript

Table of Contents

Chapter 1 – Introduction 1

1.1 Research Objectives 2

Chapter 2 – Tool Steels 3

2.1 Background 3

2.2 Classifications of Tool Steels 4

2.2.1 Non-alloy Cold Work Tool Steels 4

2.2.2 Alloy Cold Work Tool Steels 5

2.2.3 Alloy Hot Work Tool Steels 6

2.2.4 Alloy High-Speed Tool Steels 6

2.3 Heat Treatment of Tool Steels 6

2.3.1 Stress Relieving 6

2.3.2 Austenitizing and Quenching 7

2.3.3 Tempering 8

Chapter 3 – Additive Manufacturing 11

3.1 AM Techniques 11

3.1.1 L-PBF 11

3.1.2 L-DED 12

3.1.3 Feedstock Material for L-PBF and DED 13

3.1.4 The Comparison between L-DED and L-PBF 14

3.2 Microstructure and Properties of Tool Steels Fabricated by AM 15

3.2.1 Solidification and Microstructure 15

3.2.2 Mechanical Properties 16

3.3 Defects in AM Parts 18

3.3.1 Surface Roughness and Element Evaporation 18

3.3.2 Porosity 19

3.3.3 Cracking 20

Chapter 4 – Softening vs Strengthening 23

4.1 Precipitation Strengthening 23

4.2 Quantification of Particle Coarsening 25

4.3 Other Strengthening Mechanisms 26

Chapter 5 – Wear Mechanisms of Steel 29

5.1 Introduction to Tribology 29

5.2 The Wear of Steels at Room Temperature 29

5.3 The Wear of Steels at High Temperatures 30

Chapter 6 – Experimental Methods 33

6.1 Materials and Metallographic Sample Preparation 33

6.1.1 Modified H13 Hot Working Tool Steel 33
6.1.2 Tool Steels for Hardfacing 33
6.1.3 Laser Powder Bed Fusion 33
6.1.4 DED Process 33
6.1.5 Post Heat Treatment 34
6.2 Analysis Techniques 34
6.2.1 Optical Microscopy 34
6.2.2 X-ray Diffraction 35
6.2.3 Scanning Electron Microscopy 35
6.2.4 Auger Electron Spectroscopy 37
6.2.5 Transmission Electron Microscopy 37
6.2.6 Simulation Software 39
6.2.7 Mechanical Testing 39
6.2.8 Abrasive Wear Testing 40
Chapter 7 – Summary of Results 41
7.1 The Failure Mechanism of a Hot Stamping Mold 41
7.2 Modified H13 Tool Steel Manufactured by L-PBF 43
7.2.1 Effect of Post Heat Treatments on Mechanical Properties of M-H13 43
7.2.2 Effect of Post Heat Treatments on Softening Resistance of M-H13 44
7.3 Tool Steels Fabricated by DED 46
7.3.1 Defect Investigation for DED Tool Steels 46
7.3.2 Time Dependent Softening of Tool Steels by DED 48
7.3.3 Temperature Dependent Softening of Tool Steels Manufactured by DED 52
7.3.4 Wear Resistance 54
Chapter 8 – Conclusions 57
Chapter 9 – Future Work 59
Acknowledgements 61
References 63

Chapter 1 – Introduction

In recent years, more and more attention has been paid to additive manufacturing (AM) technology. Various AM techniques have been largely developed, including powder bed fusion(PBF), directed energy deposition (DED), binder jetting (BJ), laminated object manufacturing (LOM) and extrusion-based metal AM. The nomenclature may vary depending on their heat source. Compared with conventional processes, the main advantage of AM is that it can manufacture components with complex structures, and the lead time is significantly shortened. For example, when producing bones or teeth implants in the human body, AM can produce parts with nearly perfect shapes in a short time. However, in some cases, mass production is not demanded. DED is an important branch of AM technique. With a laser-beam heating source, it has many advantages including a high building rate, capability for multi-material deposition and suitability for pre-coatings on new parts or repairing damaged parts. Hence, DED is a good choice to protect/repair high-value tools, instead of being replaced.

Tool steels are also common materials fabricated by AM techniques. Two types of tool steels, carbon-free maraging steels and carbon-bearing tool steels, have been commonly investigated. For the former one, quenching during the AM process can lead to a comparably soft and ductile martensitic microstructure. Therefore, maraging steels have a decent processability in AM. High strength can be obtained by the precipitation of intermetallic particles upon aging. However, high content of Ni may stabilize austenite to room temperature and lead to austenite reversion during high temperature aging. AM of carbon-bearing tool steel is more challenging compared to maraging steels. When cooled from high temperature, a martensitic phase with high hardness and low ductility will be formed owing to the high hardenability originating from high C and alloying element content. Combined with the high thermal stress caused by rapid cooling, some defects (such as hot cracking, delamination and distortion) can be easily formed [1][2][3]. In addition, pores and lack of fusion are also common defects in AM components due to the choice of improper process parameters [4]. At present, preheating the substrate and optimizing process parameters are the major means to eliminate defects [5]. However, the AM technology for defect-free tool steel components is far from mature.

Hot work tool steel H13 having high strength with reasonable ductility, good hardenability and thermal cracking resistance is one of the widely used steels for hot stamping tools. In recent years, there have been some studies on H13 produced by laser beam powder bed fusion (L-PBF) [6][7][8]. In the published literature, most of the H13 steels fabricated by L-PBF are still inferior to the conventional H13 steels in terms of mechanical properties. Although optimizing the processing parameters can improve the quality of AM H13 parts, post heat treatments are often necessary for the as-built parts [9] in order to remove the residual stress and improve the properties. On the other hand, a slight modification of composition to H13 grade could also be a possible way to overcome these drawbacks and reach comparable properties with conventional H13.

In the carbon-bearing tool steels, H13 tool steel is the most investigated one in AM. Near fully dense and defects-free components can be produced with optimized process parameters by both L-PBF and DED. Commonly, AM-produced H13 has a martensitic microstructure consisting of fine cellular dendrite for L-PBF method and columnar dendrite with a secondary arm space of about 2-20 um for DED. Retained austenite is usually found at the cell boundaries and interdendritic region. Tempering is generally conducted on the as-printed parts to gain secondary hardening by carbide precipitation and reduction of retained austenite. However, the tensile properties of heat-treated L-PBF samples are somewhat still worse than those of conventional material. As to other high alloyed tool steels with high carbon content, the AM parts in general have a higher fraction of retained austenite. Moreover, micro segregation of alloying elements could lead to the formation of eutectic structure at the interdendritic region.

Hot forming is an important and widely used process in the automotive manufacturing segment. Tools in this process are demanded to have high strength and good wear resistance at elevated temperatures. One major problem is that the generally used hot work tool steel suffers severe wear when the tool is used to form uncoated sheet material. In this case, DED is a good choice for the manufacture of large dies and repair/refurbishment of production dies because of its freedom of material deposition. It can be used for hardfacing of the tools to delay the advent of wear or repairing the failed tools. Optimized tempering parameters should be applied to the as-built materials in order to obtain the best mechanical properties. A good understanding of the correlations between microstructure and their property is important in order to achieve good softening resistance and wear resistance at high temperatures.

1.1 Research Objectives

The objectives of this thesis are summarized as the following research questions:

(1) What is the failure mechanism of the tools in the hot stamping application? (Paper I)
(2) What are the microstructure and mechanical properties of the hot work tool steels fabricated by laser beam powder bed fusion (L-PBF) after different post-heat treatments? (Paper II)
(3) How are the defects formed and the relevant mechanisms in the tool steels produced by directed energy deposition (DED)? (Paper III)
(4) What are the softening resistance of hot work tool steels fabricated by AM after long-term exposure at high temperatures and the relevant mechanisms? (Paper II, IV & V)
(5) What are the differences in softening behavior and wear resistance between the DED and conventional tool steels? (Paper VI)

Chapter 2 – Tool Steels

2.1 Background

From the International Standard EN ISO 4957:1999, tool steel is defined as “special steels suitable for working or processing of materials, for handling and measuring workpieces and, for this purpose, exhibiting high hardness and wear resistance and/or toughness” [11]. The earliest tool steels were just ordinary carbon tool steels. The representative steel is Damascus steel, which was welded by layers of high-carbon steels and low-carbon steels [12][13]. It combines the strength of high-carbon steel with the ductility of low-carbon steels. The modern tool steels started from the Mushet special tool steel when Robert Mushet added tungsten to high carbon steel in 1868 [14]. By the beginning of the twentieth century, many complex high-alloy tool steels had been developed. In these steels, tungsten, molybdenum, chromium, vanadium and manganese were common alloying elements. Under various harsh service conditions, different tool steels were designed with high hardness and strength, good wear resistance and hot hardness as well as dimensional stability.

It is well known that alloy elements are critical for the properties of tool steels. It is necessary to have a good understanding of the metallurgical effects of these major alloy elements, which are discussed as follows.

Carbon. Carbon plays a dominant role in tool steels. It can increase the hardenability and harden the steels by forming martensite. Interstitially dissolved C atoms in the crystal lattice can efficiently inhibit the sliding of dislocation lines, which could improve the strength and hardness of steels. Cementite formed between carbon and Fe also has a similar effect. Moreover, the carbides formed by carbon and alloying elements are usually harder than cementite. Hence, these carbides can significantly increase the hardness of tool steels. In general, increasing the carbon content will increase the hardness and wear resistance, but it will sacrifice the ductility and toughness of the steels.

Silicon. Silicon is one of the main deoxidizers in the process of steel making owing to its high affinity with O. Silicon could help to improve the hardenability and softening resistance of steels. When added to hot work tool steels, silicon could contribute to the increase in hardening depth.

Chromium. Chromium in steels generally improves oxidation and corrosion resistance as well as hardenability. For cold work tool steels, chromium can form carbides to improve wear resistance. When added in hot work tool steels, chromium can increase their softening resistance and hot hardness.

Molybdenum and Tungsten. Both molybdenum and tungsten are important for hot work and high-speed tool steels. The carbides formed are extremely hard, which can efficiently prevent grain growth. This unique property makes them popular in improving high-temperature strength and hot hardness. Molybdenum can also increase the weldability and the secondary hardening capability. These two elements are widely used in high-speed steels and hot-forming tool steels.

Vanadium. Vanadium is a strong carbide former. The carbides it forms have a high hardness, which will dramatically improve the wear resistance. Vanadium also acts as a grain refiner and improves hot hardness. Hence, vanadium is popular in tool steels, especially in hot work and high-speed tool steels.

Manganese. Manganese is a deoxidizer in the process of melting. In many cases, manganese is added to steels and bound with S to decrease the detrimental effect of S on weldability. Manganese can also reduce the critical cooling rate of martensite formation during quenching. It can improve the hardenability of steels and reduce the distortion caused by quenching.

There are also many other important alloy elements (e.g., nickel, copper, cobalt, etc.) in tool steels, which will not be discussed in detail in this section.

2.2 Classifications of Tool Steels

Tool steels are often classified based on their properties and applications instead of chemical composition. According to International standards, tool steels are divided into four categories: non-alloy cold work tool steels, alloy cold work tool steels, alloy hot work tool steels and high-speed steels. The composition, properties and applications of various categories are described below.

2.2.1 Non-alloy Cold Work Tool Steels

“Non-alloy” means there is basically no other alloy elements except 0.42% to 1.25% C, 0.10% to 0.40% Si, and 0.10% to 0.80% Mn. The high hardness is attributed to the martensite phase and iron carbides, which are produced by heat treatment. Without other alloy elements, the hardening depth will be shallow, just about 3 mm. The grades such as C70U to C120 U (the number in middle represents C content in weight multiplied by 100) belong to shallow hardening steels except for C45U steel which does not need heat treatment. The CCT diagram of C90U steel (one grade of non-alloy cold work tool steel) simulated by JMatPro is shown in Figure 1a. The critical cooling rate is about 100 K/s. After water quenching, the hardness at the surface can reach 60 HRC while it decreases quickly with the distance from the surface. The low price of this type of steel makes it popular for knives, blades, hammers, etc. Non-alloy cold work tool steels shouldn’t be used at elevated temperatures (< 200 °C is suggested).

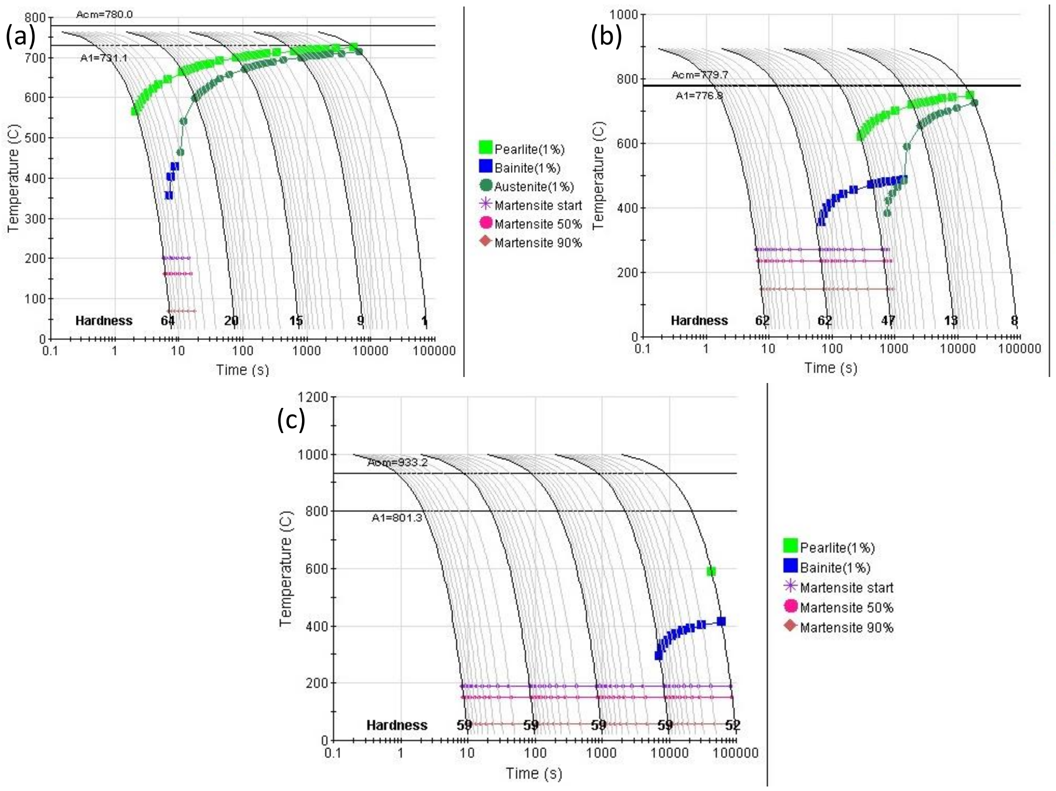

Figure 1. The CCT diagrams simulated by JMatPro using different austenitizing temperatures and grain size given in bracket for (a) C90U non-alloy tool steel (780 ℃ and 10 μm), (b) 60WCrV8 cold work tool steel (910 ℃ and 29 μm), (c) X153CrMoV12 cold work tool steel (1020 ℃ and 80 μm).

2.2.2 Alloy Cold Work Tool Steels

Compared with non-alloy tool steels, this group of steels has higher hardenability, wear resistance, and average hardness. As to the designation of alloy cold work tool steel, we can take X100CrMoV5 as an example. The starting X means at least one element is above 5 wt%. The number followed represents the C content in weight multiplied by 100. Then, major alloying elements are listed in decreasing amounts. The number at the end indicates the percentage of the alloying element having the highest amount. X100CrMoV5 represent a cold work tool steel that contains 1% C and 5% Cr. It also contains Mo and V. The excellent hardenability of this group of steels makes the martensite formation possible by quenching in the medium of oil or air. As a result, the risk of cracking and distortion dramatically decreases. Hence, they are commonly used to produce parts with large dimensions or parts that require minimum distortion. For example, X100CrMoV5 and X153CrMoV12 can be quenched in air because of their high content of Cr. As shown in Figure 1c, the critical cooling rate of X153CrMoV12 is about 0.1 K/s, which is lower than the cooling rate in air (0.3-0.5 K/s). This explains why it can be quenched in air. However, the critical rate of steel 60WCrV8 is about 10 K/s (Figure 1b). It is therefore often quenched in oil. Not only Cr, but also Mn can improve the hardenability. Steel 70MnMoCr8 with high content of Mn, for instance, can be quenched in air. Alloy cold work tool steels are widely used for cutting tools, woodworking tools, dies and forming molds. In some grades, the C content is high enough to produce graphite to provide self-lubrication, which will significantly increase the resistance to metal-to-metal wear and galling for the applications such as punches, shears, and arbors.

2.2.3 Alloy Hot Work Tool Steels

The C content in the grades of alloy hot work tool steels varies from 0.25 % to 0.60 %. Medium C content not only provides reasonably good toughness but also prevents carbide growth. Stable carbide is critical for hot work tool steels. Other alloying elements, such as Cr (0.80-5.5%), Mo (0-3.2%), V (0.05-2.1%) and W (0-9.5%), are added into these grades to increase the hardenability, making quenching in air possible. More importantly, these elements are strong carbide formers. The formation of a large number of stable carbides can provide secondary hardening and maintain microstructural stability when steels are operated at elevated temperatures.

2.2.4 Alloy High-Speed Tool Steels

High-speed steel is generally used to make tools for cutting. Due to the high cutting speed achieved, they are named high-speed tool steels. They are supposed to maintain their hardness even when being used at elevated temperatures. High-speed steel typically contains a high C content (0.73-1.40%). Other typical alloying elements are W, Mo and Co. The first generation of high-speed steel is T1 steel, which contained extremely high W content (around 18 wt.%) and was patented in the early twentieth century. The demand for low-price high-speed tool steels during the World War II led to the vigorous development of Mo-containing (replacement of W with Mo) tool steel. In general, Cr content in different high-speed tool steels is similar (3.5-4.5 wt%). The total content of W and Mo is about 10%. Interestingly, the designation of high-speed steel is different from other tool steels. It starts with HS followed by numbers separated by hyphens indicating the content of alloying elements in the order of W, Mo, V. For instance, HS6-5-2 means this high speed (HS) steel contains 6% W, 5% Mo, 2% V. Usually, high-speed tool steels have high hardness (60-67 HRC). A large fraction of stable carbides because of the high content of alloy elements is the source of both high hardness and red hardness, which provide outstanding wear resistance at elevated temperatures. Quenching of high-speed tool steels is usually performed in the medium of air, gas, or salt bath.

2.3 Heat Treatment of Tool Steels

The properties of tool steels are determined by the combination of composition (or grade) and heat treatment. The commonly applied heat treatments are stress relieving, quenching, and tempering. Suitable heat treatment of tool steels should be performed for different applications in order to obtain the required properties.

2.3.1 Stress Relieving

The purpose of stress relieving is to remove the internal residual stresses (thermal and mechanical stress). Usually, it is carried out after semi-finish machining before hardening and finish machining. Otherwise, it may lead to undesirable dimensional changes. At room temperature, when the residual stress is lower than the yield strength of the material, no distortion occurs. But when the material is heated to elevated temperatures, the yield strength will decrease and reach a level lower than the internal stress. As a result, plastic deformation occurs. This is the reason why stress relieving is needed and why it should be performed before hardening and finish machining.

In general, stress relieving is performed at temperatures between 550-700 ℃ for 1-2 hours to make sure the material is heated uniformly, and all the internal stress is relieved. In addition, the material should be cooled down slowly to avoid new internal stress.

2.3.2 Austenitizing and Quenching

Austenitizing is utilized to heat the steels and convert the ferrite to austenite. The austenitizing temperature (also known as hardening temperature) varies between 780-1250 ℃. It is dependent on the steel's composition and desired properties. The heating should be slow to avoid internal stress. Generally, several degrees per minute is recommended. To make the temperature between the surface and the center of parts uniform, one or two stops at the temperature of 600-650 ℃ or 800-850 ℃ can be set. The holding time is generally recommended to be 0.5 h. Prolonged hold time may result in grain growth. Higher austenitizing temperature is beneficial to the dissolution of C and other alloying elements in the austenite phase improving the hardenability and achieving a high hardness in the martensite after subsequent quenching. As shown in Figure 2, with the increase in hardening temperature, the final hardness after double tempering is increased. This explains why many high alloy tool steels have a high austenitizing temperature (e.g., X30WCrV9-3: 1150 ℃, HS6-5-2: 1220 ℃). However, high hardness is not the only purpose in practice. Considering low notch toughness and other difficulties caused by coarse grain size resulted from high austenitizing temperature, sometimes, the relatively low austenitizing temperature is employed. Another important factor is alloying elements. For some tool steels, ferrite stabilizer (e.g., W, Mo, Cr) in materials will shrink the austenite phase field and increase the austenitizing temperature. On the contrary, austenite stabilizer (e.g., N, Ni, Co, Mn) could extend the austenite phase field on the phase diagram, lowering the A1 temperatures. A finer grain size in the quenched parts can be achieved.

The purpose of quenching is to form martensite with high hardness. After austenitizing, a proper cooling rate should be adopted to cool down the steel to the martensite transform start temperature M_s. Too high cooling rate may cause distortion or even cracking in the components. On the other hand, too low cooling rate risks the formation of other phases instead of martensite. Hence, a compromise should always be employed. Alloying elements may shift the pearlite "nose" to the lower right direction in TTT and CCT diagrams, i.e., the formation of pearlitic or bainitic structure is delayed to longer times. Therefore, martensite can form even in thick sections at slow cooling rates. Many tool steels contain a significant amount of alloying elements to make air quenching possible, or at least easy to quench.

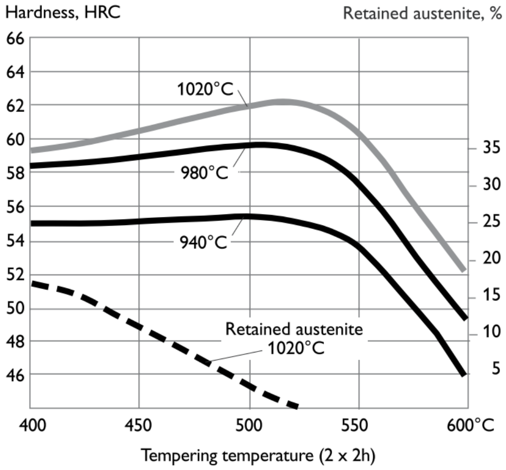

Figure 2. Tempering diagram of V4E cold work tool steel. Adapted from [15].

Alloying elements could affect the temperature range of martensite transformation. Most of the alloying elements (except V, Co, Al) lower martensite transformation temperature [15]. Higher content of alloying elements, larger decrease of M_s temperature and more retained austenite. This may cause higher internal stress due to the volume increase accompanied by martensite transformation, leading to distortion or even cracks. Meanwhile, lowered martensite transformation finish temperature (M_f) could lead to incomplete martensite transformation and a large fraction of retained austenite in quenched parts. This can explain why the retained austenite in the AM steels is always observed in the interdendritic zone with micro-segregation of some alloying elements.

2.3.3 Tempering

Tempering aims to improve the toughness of the quenched steels and to reduce or eliminate internal stress. The microstructure tends to be stabilized, and tempered martensite is formed. It is suggested that the as-quenched steels should be tempered immediately, because the internal stress in as-quenched parts could cause cracking or even fracture of the parts.

It is well known that the as-quenched martensite is brittle due to the highly distorted and stressed crystal structure caused by solute carbon atoms in body-centered tetragonal structure. During tempering, the stress is relieved, and C diffuses from martensite and forms some fine carbides. This results in an improvement in toughness, and there is no distinct decrease in hardness. Another change during tempering is the decomposition of retained austenite to form ferrite and carbides. It should be noted that when the temperature drops to lower than M_s, retained austenite can transform to brittle martensite. Therefore, second tempering is necessary to reduce brittleness. In practice, twice or three-times tempering is often performed for many tool steels.

In some high alloyed tool steels, the increase of alloying elements will extend the austenite phase region, leading to more stable retained austenite. In this case, a higher tempering temperature (typically > 500 °C) is often employed to lower the amount of retained austenite (as shown in Figure 2) and therefore higher hardness and strength can be obtained. The wear resistance of a steel depends not only on the hardness, but also on the type, size, and amount of carbides. At high tempering temperatures, carbides precipitate more efficiently from martensite and austenite. Some carbides can only be formed at 550 ℃ or higher tempering temperatures.

When selecting heat treatment parameters, hardness should never be the only consideration. The same hardness values can be obtained by different types of heat treatment. In some cases, a small amount of retained austenite may improve the fracture toughness distinctly. How to control the proportion of retained austenite and make austenite relatively stable are the key factors. Using low austenitizing temperatures can result in a small amount of retained austenite due to insufficient dissolution of alloying elements during austenitizing. This not only ensures less hardness drop but also improves the toughness of the steels. The subsequent double tempering at low temperature (maybe 180 - 250 ℃) can make the retained austenite relatively stable for future application. This strategy can be used on some cold work tool steels.

Chapter 3 – Additive Manufacturing

3.1 AM Techniques

Additive manufacturing (AM) technology has been developed over the past 30 years. It started as a technology for rapid prototyping. The early period of AM mainly focused on non-loading bearing materials, such as polymer and ceramic. The metallic AM is a newly developed field. It inherits the advantage of free designing. With this characteristic, metallic AM could produce parts with complex shapes and functional gradients which is nearly unlikely by traditional methods. Today, metallic AM technology is mainly applied in automotive, biological implants, aerospace and other fields with specific requirements [16]. Compared to conventional parts, metallurgical differences lead to some challenges (e.g., excessive residual stress, microstructural anisotropy, and common defects) for AM parts, limiting the application of AM components in various fields [16]. AM technology can be widely used in applications with a high tolerance for surface roughness such as surface hardening and medical implants, other demanding parts with high performance, such as turbine blades are at an earlier stage of development and need substantial post-processing.

The widely used AM processes can be classified into two categories: powder bed fusion (PBF) and directed energy deposition (DED). The heat source for AM includes laser beam (L), electron beam (E), gas metal arc (GMA), and plasma arc (PA). The abbreviation of heat source is often added in the designation of an AM process. Some examples are L-DED, E-DED, GMA-DED, L-PBF, and E-PBF. The three main processes are L-PBF, E-PBF, and L-DED.

3.1.1 L-PBF

L-PBF is a process to create a three-dimensional object layer by layer using a laser beam (Figure 3) from computer-aided design (CAD). A CAD file contains the information of the part produced and its support structures, which are sliced into numerous thin layers. Also, a variety of processing parameters (e.g., scanning path, thickness of layers, hatching space, etc.) are set in the CAD files [17][18][19][20]. The parts are built by spreading powder layers and melting selective regions, layer by layer within a chamber filled with inert gas. The laser beam manipulated by a galvanometer-driven mirror reacts with the metal powders resulting in melting tracks that solidify rapidly. Process parameters have a significant influence on the quality of L-PBF. For example, the porosity of the built parts can be largely affected by the volumetric energy density (VED). Too low VED could lead to lack of fusion, while too high could produce keyholes. Even the scanning strategy could significantly change the phase constitution in L-PBF parts. Kudzal et al. [21] reported that using the strategy of outside-in concentric rings, the austenite content in the parts of PH17-4 steel was much higher (82%) than that of regular scan strategies (~50%). Since the mechanism of L-PBF is similar to L-DED, more details will be discussed in Section 3.1.2.

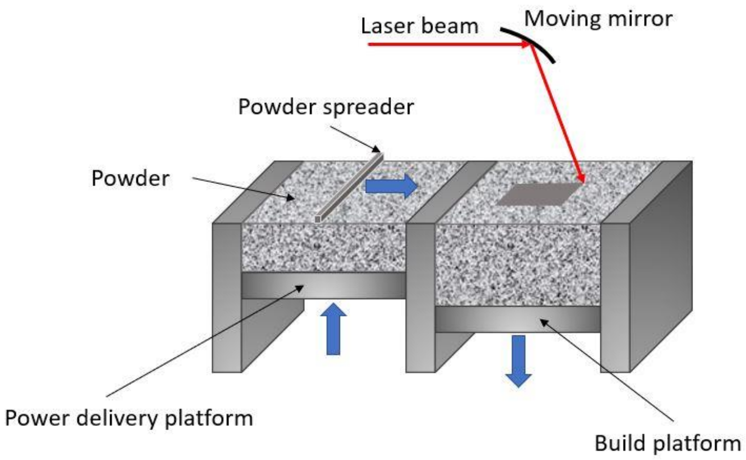
Laser beam
Moving mirror
Powder spreader
Powder
Power delivery platform
Build platform

Figure 3. Schematic diagram of L-PBF.

3.1.2 L-DED

L-DED, also called laser cladding, is a process in which metal powder/wire from a nozzle is fused onto a metal surface by the focused beam of a high-power laser in a protective atmosphere. In this thesis, the feedstock material is metallic powders, and the heating source is laser beam. DED refers to metal powder directed energy deposition by laser beam in the following text. The schematic diagram of such a DED process is shown in Figure 4. The powder is delivered coaxially with a laser beam and protected by shielding gas such as argon. Similar to most of the AM processes, a CAD file is used to guide the fabrication of components. The overhanging features in the part may require supporting structures to avoid distortion caused by heat and their weight [39]. The processing parameters, such as scanning speed of the laser beam and the feed rate of the powder, are either pre-set or adjusted in the process. DED technology is often used to produce components with rough blank shapes requiring post-machining to achieve the desired geometry and surface quality.

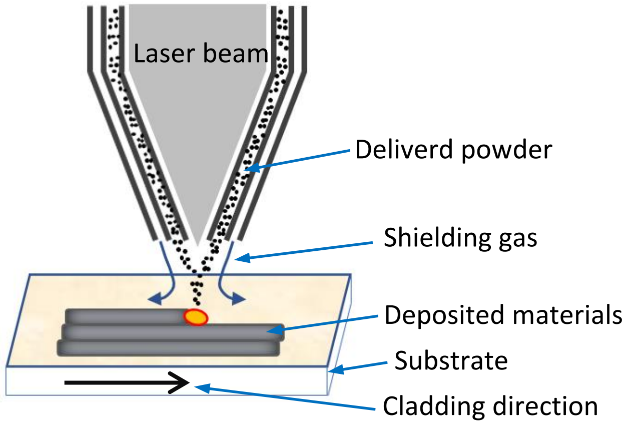
Laser beam
Deliverd powder
Shielding gas
Deposited materials
Substrate
Cladding direction

Figure 4. Schematic of directed energy deposition.

Similar to L-PBF, the quality of DED parts is also affected by its process parameters, such as laser power, layer thickness, scanning velocity, hatching space etc. Also, these parameters interact with each other. The influence of some parameters is discussed in the following text.

Laser power. Power is a critical parameter, which will significantly impact the melt pool size, penetration depth, defects, cooling rate, evaporation of alloy elements and so on. With higher power, the size of the melt pool will increase because of larger heat input. The benefit is the sufficient melting of the powder, leading to dramatically reduced lack of fusion and consequently increased density of the builds. The cooling rate is also affected by the power level. High power will decrease the cooling rate and consequently the thermal stress during the solidification, minimizing the tendency of cracking. On the other hand, too high power should be avoided, because it increases the temperature of melt pool, accelerating the vaporization of alloying elements. Meanwhile, the recoil pressure caused by vaporization could eject the molten droplets from the melt pool [33][34]. Power is not the only factor that determines the heat absorbed in a melt pool. Power density distribution and energy absorption coefficient are also important characteristics of heat source. Generally, the power density distribution P_d of a laser beam follows the Gaussian profile.

Scanning speed. Generally, the scanning speed is coupled with the power of the heat source (P). For a fixed heat input, scanning speed is inversely proportional to the power. Increasing the scanning speed will decrease the volumetric energy density (VED), which can be defined in Equation (1):

$$VED = \frac{P}{v*h*t} \tag{1}$$

Where v is the scanning speed, h is the hatching distance between the neighboring tracks, and t refers to layer thickness. It is seen from Equation (1) that the melt pool will be elongated, narrow and shallow at the condition of constant VED and high scanning speed. Continuous increase in the scan speed will increase the trend of lack of fusion, similar to decreasing power. This is accompanied by high cooling rates, which will increase the susceptibility to cracking. Although high scanning speed increases the yields of printed parts, a compromise should be made for ensuring quality.

To obtain high-density parts, many other aspects should also be taken into consideration, such as scanning strategy, processing atmosphere, preheating, and powder layer thickness. Three critical indices related to the melt pool dimension (melt pool depth D, width W, and length L) are the ratio of a depth-to-layer thickness (D/t), width-to-hatching space (W/h), and length-to-width (L/W) [36]. It has been reported that relatively high density is generally obtained in the index range of $1.5 < D/t < 2$, $1.5 < W/h < 2.5$ and $L/W < 2\pi$ [37][38]. The process parameters are material dependent and need further exploration.

3.1.3 Feedstock Material for L-PBF and DED

It is generally believed that the quality of built parts is influenced by the characteristics of alloy powders used. The relationships between powder characteristics (e.g., particle morphology, size distribution, chemical composition) and the resulting part properties has been discussed in many publications [22][23][24]. In the reference of [25], when decreasing the powder size of 316L stainless steel in L-PBF, the powder packing density is increased, leading to a higher part density and surface quality. On the contrary, shifting the powder size distribution to coarser direction, the printed parts had a higher elongation at fracture [26]. In addition, the irregular shape and wide size distribution worsen the surface quality of the parts produced [27]. The powder degradation is detrimental to the quality of fabricated L-PBF parts. Fiegl et al. [28] reported that long-term reused AlSi10Mg0.4 powder could cause 4-times higher porosity and distinct worse tensile properties than the sample made by virgin powder.

The characteristic of powder also significantly influences the quality of DED products. For instance, the powder with internal pores could inherit its porosity to the built parts. Large powder particles lead to high surface roughness [29]. Uniform size distribution and smooth surface of the powder can promise a good flowability and a stable melt pool size during DED [30]. In addition, the powder feeding is controlled by both gravity and carrier gas, the latter of which could be trapped into melt pool and form porosity in the built parts.

The quality of the powders largely depends on the manufacturing methods. Normally, the powders produced by plasma atomization and gas atomization are popular because of their good sphericity and lower porosity. Despite of high powder quality from plasma atomization, the high cost and low yield make it less attractive from economic point of view. The powder produced by water atomization is also used in some cases. One advantage of AM technology is the optimized usage of raw materials. This is meaningful considering the limited resources on our planet. Typically, the powders utilized in the building process is just a small fraction and rest of the powder will be recycled. In industrial AM practice, the powders may be reused more than a few tens of times. However, the reused powders deteriorate even in vacuum or inert gas environment. Aggravated oxidation, agglomeration of powders and the change of chemical state of powder surface may occur. For instance, the thickness of oxide layer on used copper powders is greatly dependent on the purity of the powder. High purity could lead to a relative thin oxide layer [31]. Surface roughening, particle sintering, and element evaporation were found on the reused Ti-6Al- 4V powders after EB-PBF process [32]. The quality of reused powder should be considered because it will influence the properties of the built components, especially for oxygen-sensitive materials such as Titanium alloys. The correlation between powder characteristics and printed parts is complex.

3.1.4 The Comparison between L-DED and L-PBF

Forming a melt pool using laser beam is the fundamental for both DED and L-PBF technology. Theoretically, the mechanism is similar to that of welding. However, many differences exist between DED and L-PBF. Table 1 presents a comparison between L-DED and L-PBF technology. In most cases, DED has a higher laser power than that of L-PBF, making the melt pool in DED larger than in L-PBF. Consequently, the dimensional accuracy of DED is not as good as L-PBF [35]. Nevertheless, laser power is a major factor that influences building efficiency. Larger melt pool will increase the building efficiency if the powder feed rate is increased correspondingly. Compared to L-PBF, DED technology is more convenient to manufacture larger dies and repair/refurbishment of production dies thanks to its freedom of material deposition. It is also more effective when developing functionally graded materials.

Both DED and L-PBF are capable of manufacturing parts with complex shapes that are difficult to machine or build by conventional methods. The selection of AM technique is dependent on the dimensional tolerance, build size, mechanical properties, and the acceptance level of defects. Considering the opportunity offered by these techniques, in-depth knowledge regarding processing, microstructure and properties is of great importance for tool steels.

Table 1. Comparison of directed energy deposition by laser beam (L-DED) and laser powder bed fusion (L-PBF) [35].

Process	L-DED	L-PBF
Heat source	Laser	Laser
Powder delivering type	Coaxial delivering	Pre-spread powder layer
Power (W)	100-3000	50-1000
Speed (mm/s)	5-20	10-1000
Max. build size (mm*mm*mm)	2000*1500*750	500*280*320
Dimensional accuracy (mm)	0.5-1.0	0.04-0.2
Surface roughness(µm)	4-10	7-20

3.2 Microstructure and Properties of Tool Steels Fabricated by AM

3.2.1 Solidification and Microstructure

The solidification and microstructure of the parts fabricated by AM are affected by many processing parameters. Temperature gradient G (K/mm) and growth rate R (mm/s) are the most important physical quantities in solidification, which determine the morphology and size of microstructure in the as-built state. Figure 5 shows the influence of G/R and G×R on the solidification microstructure. With a decreased ratio of G/R, the morphology will change in the sequence of planar → cellular → columnar dendrite → equiaxed dendrite. On the other hand, the higher G×R value (essentially this is the cooling rate) will lead to a finer structure. The cooling rate in AM process is generally higher than that in the traditional casting. Usually, it is in the range of 10^3 -10^5 K/s for DED and 10^5 -10^7 K/s for L-PBF, respectively. Consequently, the microstructure in AM metal parts is finer than that in traditional ones. Due to the difference of the cooling rate in DED and L-PBF, the morphology in metals manufactured by L-PBF is usually cellular, which is different from the columnar dendrite or mixture of cellular and columnar dendrite in the ones produced by DED.

During solidification, grains in metal tend to grow along the heat flow direction which is usually perpendicular to the melt pool boundary. However, this direction is different in L-PBF and DED. The melt pool in L-PBF is long and shallow due to its high scanning speed. This geometry leads to a nearly vertical growth of the grains, i.e., roughly along the building direction, as indicated by the arrows in Figure 6a. Relatively larger power and smaller scanning speed make the melt pool in DED deeper compared to that in L-PBF, as shown schematically in Figure 6b. The grains may grow deviating from the building direction due to local curvature of the solid/liquid interface as indicated by the arrow in Figure 6b. Consequently, the grain orientations in the component fabricated by DED usually have a relatively large angle with respect to the building direction. Another phenomenon is the “competitive” grain growth. At the early stage of solidification, extensive grains with different orientations are nucleated due to the large nucleation rate. Only the grains with the orientation parallel to the heat flow direction have a high chance to survive.

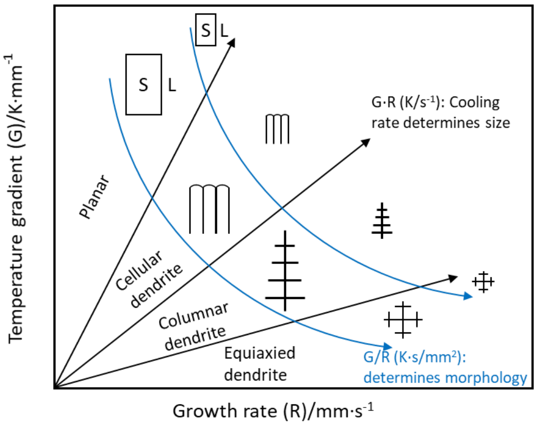
Temperature gradient (G)/K·mm⁻¹
Growth rate (R)/mm·s⁻¹
S L
S L
Planar
Cellular dendrite
Columnar dendrite
Equiaxied dendrite
G·R (K/s⁻¹): Cooling rate determines size
G/R (K·s/mm²): determines morphology

Figure 5. The influence of temperature gradient and growth rate on the morphology and size of solidification microstructure. Adapted from [8].

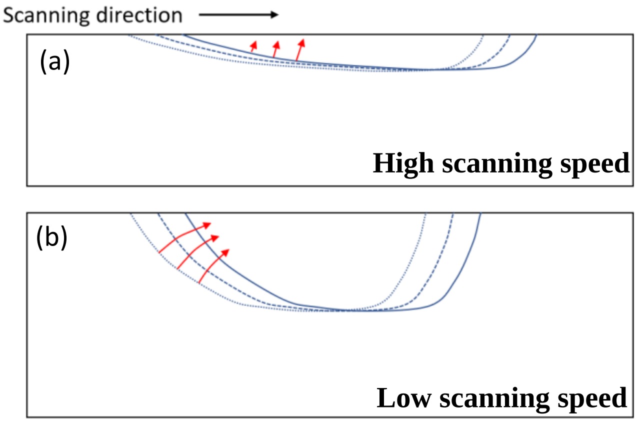
Scanning direction
(a)
High scanning speed
(b)
Low scanning speed

Figure 6. Schematic illustration of grain growth direction under different scanning speeds. (a) high scanning speed, (b) low scanning speed. Adapted from [35].

3.2.2 Mechanical Properties

High cooling rate leads to a fine microstructure. AM parts are thus expected to have excellent mechanical properties. In fact, AM parts after post heat treatment have a comparable or even higher strength than conventional parts often at the expense of ductility. The high strengths are attributed to the potentially high dislocation density caused by rapid solidification and residual stresses. The low ductility in AM metal parts originated from the combined effect of high dislocation density, internal defects such as sharp lack-of-fusion or uneven microstructure between the boundary and center of the melt pool [40]. Processing parameters affect mechanical properties. Low volumetric energy density results in a small melt pool, fast cooling rates and fine structures compared to the parts fabricated with high volumetric energy density. This will lead to high yield and ultimate tensile strength (UTS) in the materials.

Since tool steels are the target material of this thesis, the discussion here will focus on the mechanical properties of AM tool steel including hot work tool steels, cold work tool steels and high-speed tool steels. H13 hot work tool steel has been extensively studied. The typical mechanical properties reported for AM H13 are shown in Table 2. The hardness ranges from 530 HV to 670 HV in L-PBF parts, which is comparable or even higher than wrought H13. The reasons behind this could be less retained austenite in the printed parts due to the intrinsic tempering by the neighbor layers and the finer cellular structure caused by fast cooling. The yield strength and UTS of the as-built parts are usually lower than wrought one owing to the brittle martensite. The elongation is also low in the L-PBF produced H13 due to the same reason, indicating further heat treatment is needed. After tempering, the strengths have a significant improvement and are close to the wrought counterparts. Chadha et al. [41] investigated the influence of austenite on the tensile properties of L-PBF H13 and found that the quenched and tempered sample exhibits higher tensile strength, but lower elongation as compared to the as-printed sample. In the case of DED, the hardness of as-cladded parts ranges from 460 HV to 660 HV. It is hard to prepare tensile specimens due to the small thickness, so only limited data on tensile properties of DED H13 is available in literatures. According to [47], the yield strength and UTS of DED H13 material are close to the wrought one. The elongation in these parts is relatively low (5-6 %) and needs distinct improvement. In addition, it presents an even better wear resistance than conventional counterparts in the pin-on-disc test. Compared to L-PBF, it seems the mechanical properties of H13 parts made by DED are promising.

Table 2 Overview of mechanical properties of AM H13 steel. AP: as printed, AH: tempered, PH: pre-heated baseplate.

Condition	YS (Mpa)	UTS (Mpa)	δ (%)	Hardness	Ref.
H13 wrought AH	1569-1650	1930-1990	9-12	40-53 HRC.	[42][43][47]
L-PBF AP		1000-1200	0.8-1.9	612 HV	[44]
L-PBF AP	1150-1275	1550-1650	1.5-2.25		[45]
L-PBF AP	1236	1712	4.1		[43]
L-PBF AP (PH: 200 ℃)	835	1620	4.1		
L-PBF AP (PH: 400 ℃)	1073	1965	3.7		
L-PBF AP	1003	1370	1.7	59 HRC	[42]
L-PBF AH	1580	1860	2.2	51 HRC	
L-PBF AP (PH: 240 ℃)	892	1440	1.5	571-579 HV	[46]
DED AP	1288-1564	2033-2064	5-6	660 HV	[47]
DED AP				46-54 HRC	[48]
DED AP				550 HV	[49]
DED AP				400-600 HV	[50]
DED AP				53-56 HRC	[51]

Usually retained austenite is observed in as-printed AM parts in many tool steels such as cold work tool steels X65MoCrWV3-2 [53], high-speed steels M2 [54][55] and M3.2 [56] due to their high content of C and other alloy elements. Hence, the hardness in the as-printed state is probably lower than its conventional counterparts. For instance, cold work tool steel D2 produced by DED has a hardness of 43-45 HRC [51], which is significantly lower than that of wrought D2 (58 HRC) [52]. In addition, a higher hardness is obtained at the bottom layers than the top layers due to the intrinsic tempering during the process. Figure 7 shows the hardness profile of a cold work tool steel, V4E, fabricated by DED. The top layer has a hardness of 710 HV, which is lower than the hardness of the layers below due to lack of intrinsic tempering. After a double tempering at 550 ℃ for 3h, the hardness can reach the values as high as ~ 920 HV due to the removal of retained austenite and secondary hardening.

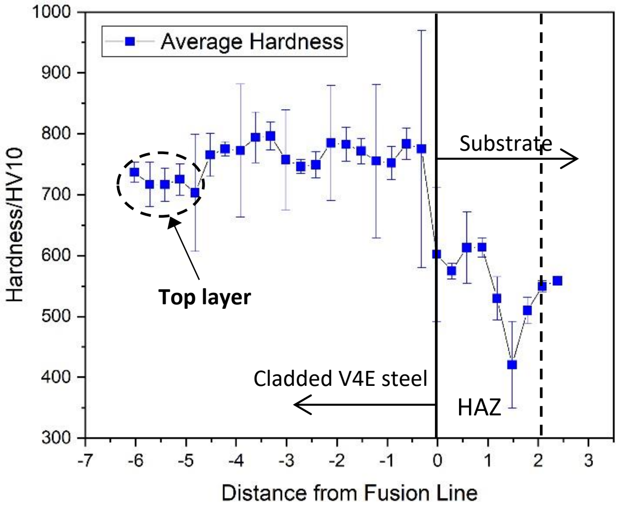

Figure 7. Hardness profile of V4E cold work tool steel produced by DED. HAZ is heat affected zone of the substrate.

3.3 Defects in AM Parts

Defects are a common topic in AM field. Cracks and voids are the major defects of concern in AM parts. Before focusing on these two types of defects surface roughness and element evaporation will be discussed first.

3.3.1 Surface Roughness and Element Evaporation

Evolution of surface roughness is a complex phenomenon. It could be caused by both the intrinsic fluctuation of melt pool shape and the balling or partially melted particles on surface. It is related to the melt pool size, powder particle size and processing parameters[57][58]. Kempen [55] reports that remelting is an effective way to improve surface quality. Indeed, it can improve both the relative density and surface quality of L-PBF fabricated M2 steel. The arithmetic mean surface roughness decreases from 18.3 µm to 8.6 µm. Meanwhile, the porosity and particles on surface are extensively eliminated.

Element evaporation, also referred as loss of alloying elements, takes place during AM process when the melt pool temperature is high. The consequence is the changes in composition which will affect the solidification microstructure and mechanical properties [59]. Therefore, it can be a serious issue for high-quality demanding parts. Usually, the vapor flux is proportional to the equilibrium vapor pressure, which is strongly dependent on temperature and elements. The selection of processing parameters, such as high power and low scanning speed, can increase melt pool temperature which will in turn increase the vapor flux. However, a “counterintuitive” finding was reported [60] that a higher aluminium content was obtained at the “slow and hot” condition during the DED process of Ti-6Al-4V. It is explained by a low surface-to-volume ratio in a big melt pool that leads to less compositional variation.

3.3.2 Porosity

Porosity is common in AM parts, and it should be avoided as much as possible due to its detrimental effect on mechanical properties. Generally, porosity in AM parts can be categorized into three types: lack of fusion, voids from keyholes and trapped gas pores.

Lack of fusion is caused by insufficient melting and consequently incomplete adherence to the previous layer or track. It is related to the ratio of melt pool depth to layer thickness, which can be used as an index for lack of fusion [59]. The voids of lack of fusion often present an irregular shape at the lower position of melt pools. Adjusting the processing parameters that increase the melt pool depth or decrease the layer thickness can minimize the tendency of lack of fusion. It has been experimentally proved that high heat input by increasing laser power or decreasing scanning speed can effectively reduce or even eliminate the porosity caused by lack of fusion [59][61][62]. Additionally, adjusting hatch spacing to obtain a proper bonding to the previous track is also an effective way to reduce lack of fusion [63]. In some cases, the voids in melt don’t have enough time to float upward to the melt pool surface. Therefore, the surface tension and viscosity of a metallic liquid are important factors as well. Moreover, melting temperature and thermal conductivity, which could influence the dwell time of the melt pool, also affects the formation of lack of fusion.

Keyhole porosity originates from the tip of the keyhole. Essentially, keyhole is not a type of defect. It’s formed in the liquid melt pool when the strong recoil pressure from the rapid evaporation of the metal pushes the surrounding molten liquid downward, as shown in Figure 8 [64][65]. During the high-power density melting, the shape of keyhole will become narrow but deep, and the tip will be unstable. Without proper control, the tip could collapse from keyhole and be trapped by the solidification. The size of keyhole porosity depends on the size and shape of keyhole.

Trapped gas pores could be from either powder particles or trapped shielding gas in melt pool. The pores usually present a spherical shape. In laser AM techniques, inert gas such as argon and helium are often employed as shielding gas. Usually, these gases are insoluble and don’t react with liquid metals [66]. When trapped into the liquid, inert gas either floats out of melt pool or is left inside solid after solidification. However, it will not change the composition of molten alloy. When using nitrogen as shielding gas, situation is different because nitrogen can dissolve into metal liquid before floating out or being trapped by solidification. How this affects the properties is material related. For L-PBF 316L stainless steel, only limited differences are shown when comparing nitrogen and argon [67]. But for some metal such as Ti-6Al-4V, nitrogen shielding gas could react with liquid metal and leads to deterioration of properties [67].

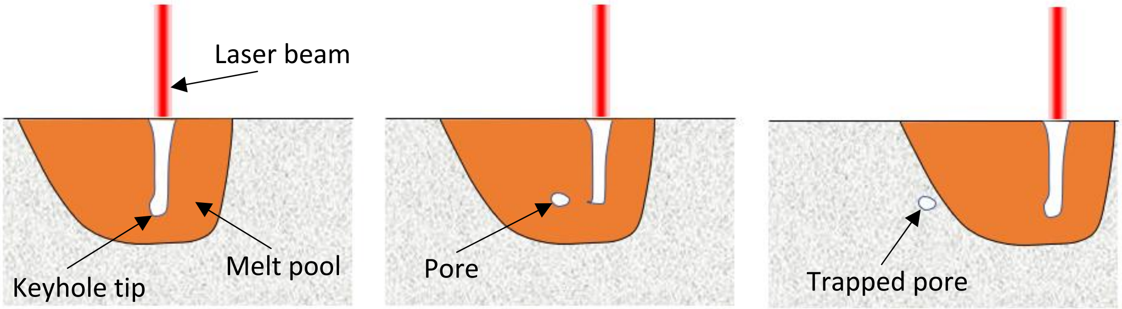

Figure 8. Keyhole porosity formation from the instable keyhole tip. Reproduced from [65].

3.3.3 Cracking

Cracking in AM parts includes delamination and hot cracking. In this thesis, we focus on hot cracking, also known as solidification cracking, which is caused by uneven contraction during solidification. In an AM process, the temperature of the new built layer is higher than that of the previous layer (or substrate). Hence, the contraction caused by cooling in the new layer is more than that in the previous layer, leading to a tensile stress in the new layer. If the tensile stress is high enough, hot cracking will initiate at the weak places. This tensile stress caused by temperature change is named as thermal stress (σ). It is determined by three factors[68]: temperature change (ΔT), elasticity modulus E and thermal expansion coefficient (α), as given in Equation (2):

$$\sigma = E\,\alpha\,(T_f - T_o) = E\,\alpha\,\Delta T \tag{2}$$

where T_f, T_o represent final and initial temperature of solid respectively. It is seen from Equation (2) that materials with a high thermal expansion coefficient α will have a relatively high thermal stress σ during the cooling process. To avoid cracking, thermal stress should be minimized, and the threshold strength of tearing should be increased. There are two basic routes, i.e., composition control and processing parameter tuning, to improve the resistance to hot cracking. The former one focuses on metallurgical factors to reduce the temperature range of solidification, especially the temperature range of the last stage of solidification.

Regarding compositional aspect, a cracking criterion was proposed by Kou [69]. It is based on the maximum slope of $|dT/df_s^{1/2}|$ in the last stage of solidification, which corresponds to a specific solid fraction f_s, 0.95 for instance. The term of $|dT/df_s^{1/2}|$ is the susceptibility of cracking and can be expressed in Equation (3) [69]:

$$\left|\frac{dT}{df_S^{1/2}}\right| = \frac{2(1-k)(T_m-T_E)\sqrt{1-f_E}}{f_E} \tag{3}$$

where k is partition coefficient, T_m is the melting temperature of matrix, T_E is the eutectic temperature, f_E is the faction of eutectic structure. Figure 9 compares the predicted hot cracking susceptibility by Equation (3) and experimentally measured crack density of Al-Si binary alloy. Two curves show almost the same trend except the difference of Si concentration for the highest susceptibility. In order to resolve this discrepancy, Liu and Kou [70] suggested that the effect of solid-state diffusion should be taken into consideration. An additional dimensionless parameter α including the effect of diffusion is employed, which is expressed in Equation (4) [70]:

$$\alpha = \frac{4D_s t_f}{\lambda_2^2} \tag{4}$$

Where D_s is the diffusion coefficient of the solute in solid matrix, t_f is freezing time, λ_2 is the secondary dendrite arm spacing. With this, f_s can be expressed as Equation (5), where T is the temperature of melt, C_0 is the concentration of solute, and m_L is the slope of the liquidus [70]:

$$f_s = \frac{1}{1-2\alpha' k}\left[1-\left(\frac{T_m - T}{-m_L C_0}\right)^{\frac{1-2\alpha' k}{k-1}}\right] \tag{5}$$

where α′ is expressed as:

$$\alpha' = \alpha\left[1-\exp\left(-\frac{1}{\alpha}\right)\right] - \frac{1}{2}\exp\left(-\frac{1}{2\alpha}\right) \tag{6}$$

Adopted from [71], D_s is chosen from 2×10^{-9} to 9×10^{-9} m^2/s, which is consistent with the self-diffusion coefficients below the melting temperature and the predicted result is consistent with the experimental results.

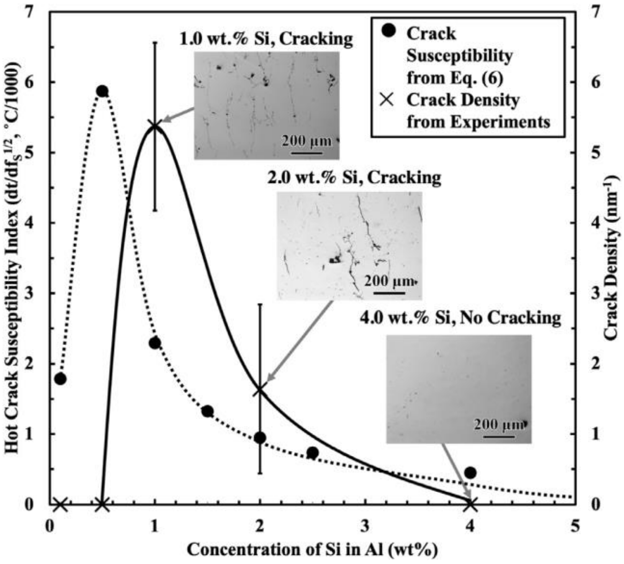

Figure 9. Hot cracking susceptibility prediction vs. experimentally measured crack density for binary Al-Si alloys (Reproduced with the permission of Elsevier [71]).

In most cases, the composition of an alloy is fixed. Therefore, tuning the processing parameters is a realistic means to avoid cracking. According to Equation (2), increasing the final temperature of the component can decrease the temperature change ΔT during the cooling process, which in turn reduces the thermal stress correspondingly. Preheating the baseplate is an effective way to avoid hot cracking [10]. High preheating temperature above the martensite start temperature M_s will prevent the martensite transition [72] and leads to transformation of austenite to upper bainite [73]. Preheating can also decrease the thermal gradient G and the cooling rate. Hence, the dimensionless parameter α in Equation (4) will increase accordingly, which will help to decrease the hot cracking susceptibility.

It is believed that the fine and isotropic microstructure is beneficial to high tearing resistance. Epitaxial growth and the coarse columnar dendrites are undesirable. Obviously, high cooling rate can help to obtain a fine structure. Another strategy for a fine microstructure is to use nucleating agents which increases nucleation rate during solidification in an AM process. Martin et al [74] incorporated TiC nanoparticles into 7075 and 6061 Al alloy powders. A crack-free, fine-grained microstructure was obtained. The final strengths are comparable to wrought materials. However, to find a suitable nucleating agent is not an easy task. According to the classical nucleation theory, low-energy nucleation barrier requires a match of the crystallographic lattice spacing and densities.

Chapter 4 – Softening vs Strengthening

Metal softening may occur when the materials are subjected to high temperature exposure. This is accompanied by the change of the microstructure including phase constitution, grain size, lattice defects density and so on. Even when cooled to room temperature, the material is softer than before. The softened material can no longer withstand the previous load, which may cause accidents in engineering applications. Quantification of softening resistance of steels is a challenging research topic as it requests combined knowledge of strengthening mechanisms (e.g., precipitation strengthening, solid solution strengthening, dislocation strengthening and grain boundary strengthening). It is difficult to find the experimentally the accurate parameters for these strengthening models. In the following text, important strengthening models will be discussed.

4.1 Precipitation Strengthening

Precipitation hardening is one of the most effective methods for developing high-strength steels. The fundamental principle is that some secondary precipitated particles act as obstacles to hinder dislocation movements. The interaction between dislocations and precipitates will be changed with the growth of precipitates. At the initial stage of precipitate formation, small and soft precipitates will be sheared by dislocation. Extra stress is needed, leading to hardening. When a particle with a diameter $\bar{d}_p$ is sheared by a dislocation, the work done is $\tau_{shear} b x \bar{d}_p$, where b is burgers vector and x is the separation between particles. An extra interface (faulted plane) between the particle and matrix is created. It requires surface energy equal to $\pi(\frac{\bar{d}_p}{2})^2\sigma$, where σ is the specific surface energy between the precipitate and matrix. These two parts, i.e., work done by dislocation movement and surface energy, should be in balance, as given in Equation (7) [75]:

$$\tau_{shear} b x \bar{d}_p = \pi(\frac{\bar{d}_p}{2})^2\sigma \tag{7}$$

The volume fraction of the particles can be expressed as a function of particle separation *x* and particle diameter $\bar{d}_p$, as given in Equation (8) [76]:

$$f_v = \left(\frac{4}{3}\pi\,(\frac{\bar{d}_p}{2})^3\right)/x^3 \tag{8}$$

Using Equation (7) and Equation (8), the expression of τ_{shear}can then be obtained, as exhibited in Equation (9):

$$\tau_{shear} = (\frac{3}{4}\pi)^{1/3}\cdot\frac{\pi\sigma}{2b}\cdot {f_v}^{1/3} \tag{9}$$

The necessary shear stress τ_{shear} is only a function of the fraction of particles. It is known that precipitation is a process of nucleation and growth. With time, both the size and fraction of precipitated particles increase. As indicated by Equation (9)., the stress for particle shear (τ_{shear}) will increase with the fraction of the precipitates correspondingly. Once the fraction of precipitates reaches the maximum, an equilibrium value predicted by phase diagram, the stress required for particle shear becomes constant, as shown in Figure 10. With prolonged time, the average particle size will increase but the total fraction has no change. This corresponds to coarsening of the precipitates. The particle size at which coarsening starts is marked as d_{co} in Figure 10.

Another strengthening mechanism is Orowan looping for hard and relatively large precipitates, by which dislocation lines will be bended and form loops around the particle. However, additional stress τ_b required for Orowan mechanism decreases with the particle size. It can be quantitative represented by Equation (10) and (11) [75][76]:

$$\tau_b \approx Gb/x \tag{10}$$

$$x = \sqrt{\frac{2\pi}{3f_v} \cdot \frac{\bar{d}_p}{2}} \tag{11}$$

where G is the shear modulus of matrix, b is the Burgers vector, x is the particle spacing determined by average diameters of precipitates $\bar{d}_p$ and their volume fraction f_v.

It can be clearly seen from Equation (10) and (11) that with the increase in particle size, the necessary stress τ_b for Orowan looping will decrease. On the other hand, the stress required for particle shear τ_{shear} increases with particle size until the volume fraction of precipitates reaches the equilibrium value. There is therefore a critical particle size (d_c) at which $\tau_b = \tau_{shear}$. When $\bar{d}_p < d_c$, particle shear is governing. When $\bar{d}_p > d_c$, Orowan looping is dominant. The transition from particle shear to particle looping will inevitably occur with the increase of particle size. The stage with particle size larger than the critical value corresponds to softening stage.

Notice softening does not strictly correspond to coarsening of the precipitates. Softening starts when particle size $\bar{d}_p$equals to critical value d_c and Orowan looping plays an overriding role. Coarsening starts at $\bar{d}_p = d_{co}$ when the volume fraction of precipitates reaches the maximum and becomes constant. Softening may occur before coarsening (Figure 10a) or after coarsening (Figure 10b). In the first case ($d_{co} > d_c$), the strength goes down prior to the completion of precipitation. This means the size and volume fraction of precipitates may still increase when softening occurs. In the second case ($d_{co} < d_c$), there exists a plateau before Orowan looping mechanism takes effect. However, in most case, d_{co} and d_c differ not much. Softening and precipitate coarsening are often equated by researchers.

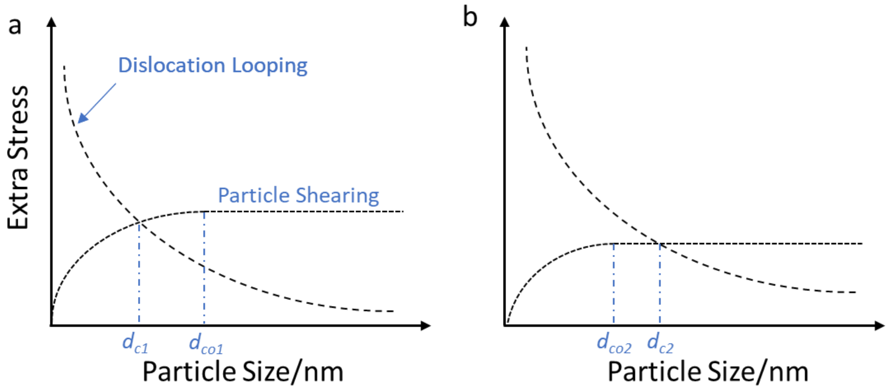

Figure 10. The competition between particle shear and dislocation looping mechanisms: (a) material softening before precipitate coarsening; (b) precipitate coarsening before material softening. d_c: Critical diameter. d_{co}: Coarsening diameter.

4.2 Quantification of Particle Coarsening

In this thesis, one of the major focuses is the softening of steels. Hence, the particle size during the heat treatment is critical. When precipitates grow, necessary elements diffuse from the surrounding supersaturated matrix. When coarsening, the volume fraction of precipitates is constant and big particles grow at the expense of small particles. This process is known as Ostwald ripening. As we known, the smaller the particle size, the larger the surface energy. Hence, in order to lower the Gibbs energy of the system, the small particle tend to dissolve, and the big particle tend to grow up. The rate of this process is controlled by the interfacial energy and the diffusion of the necessary elements. Generally, the relationship between particle size r and coarsening time t follows Equation (12) [77]:

$$r^n - r_0^n = A \cdot t \tag{12}$$

where n is the coarsening exponent, A is a constant depending on models for coarsening. So far, there is no perfect model that gives a perfect simulation. Classic Lifshitz-Slyozov-Wagner (LSW) theory [78][79] is the most widely used one., in which the coarsening exponent n is 3, and A can be express as:

$$A = \frac{8}{9}\frac{D\sigma}{RT} c_m V_m^p \tag{13}$$

where D is the diffusion coefficient of the controlling elements, R is the gas constant, T is temperature in Kelvin, c_m is solid solubility of the controlling elements in matrix, V_m^p is the mole volume of precipitate. However, one of the limitations of LSW theory is that the fraction of precipitates should be very small (< 1 vol%). When the material has a relatively large volume fraction, constant A should be modified. Taking the influence of volume fraction into account, Equation (14) could be revised in the below form [80]:

$$A = \frac{8D\sigma V_m^p}{9RT} \cdot \frac{6c_m(1-c_m)f_v}{(c_p-c_m)^2} \tag{14}$$

where c_p is the concentration of the controlling elements in precipitate. Using this modified model, the calculated results agree well with the experimental results [80].

Another critical factor that may influence the simulation is the diffusion coefficient D of the controlling elements. It is well known that the temperature has a significant influence on diffusion coefficient following Arrhenius equation. In addition, lattice defects (e.g., dislocation, grain boundary) in materials act as shortcut paths and accelerate diffusion. Dislocation diffusion is also named as pipe diffusion with D several orders higher than that of bulk [81]. The coefficient of bulk diffusion can be obtained from literatures. Based on reference [82], the amplified factor α_{dis} for pipe diffusion and α_{GB} for grain boundary diffusion with respective to the bulk diffusion can be expressed as:

$$\alpha_{dis} = 1.33 \times 10^{-2} \times \exp\left(115000/(RT)\right) \tag{15}$$

$$\alpha_{GB} = 2.53 \times 10^{-2} \times \exp\left(132700/(RT)\right) \tag{16}$$

Using Equation (15) and Equation (16), the diffusivity of Mo in bcc Fe can be calculated and plotted in Figure 11. As we can see, the diffusivity through dislocation line is about 3 to 5 orders higher than that in bulk material. Diffusion at grain boundary is one more order higher than that via dislocation. Indeed, the diffusion in the metallic materials with high density of dislocation or grain boundary will be significantly quicker than that in full-annealed or equilibrium state. High diffusivity will increase the coarsening rate of the precipitates. In summary, the rate of precipitate coarsening is not only determined by the intrinsic diffusion coefficient of controlling elements, but also related to the location of particles, heat treatment state, and so on. All in all, the diffusion coefficients will significantly influence the softening resistance of the investigated materials.

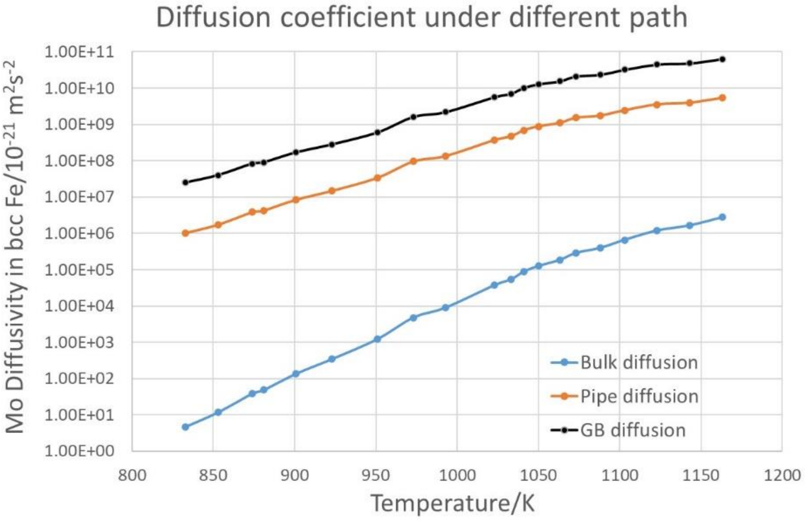

Figure 11. The diffusion coefficient of Mo in bcc Fe with different diffusion mechanisms.

4.3 Other Strengthening Mechanisms

Besides precipitate strengthening, other strengthening mechanisms are also important. Dislocation strengthening is one of them. The fundamental mechanism is that the strength of the material can be improved by the stress field created by dislocations which hinder the movement of other dislocations through both repulsive and attractive force. In addition, entanglements will occur if two or more dislocations cross each other. These entanglements can hinder the motion of not only the tangled dislocations, but also other dislocations. Therefore, a higher external stress is needed for deformation, leading to increased strengthen of the material. Dislocation density ρ determines the extent of strengthening effect, as expressed in Equation (17) [83]:

$$\sigma_{dis} = M\alpha Gb\sqrt{\rho} \tag{17}$$

where M is the Taylor factor (2.75 for bcc metals), α is a constant (0.38 for bcc iron), G is the shear modulus, b is the Burgers vector. Dislocation density ρ can be evaluated by both XRD using Williamson-Hall and Warren-Averbach (MWHWA) methodologies, and TEM techniques using Equation (18):

$$\rho = 2N/Lt \tag{18}$$

where N is the number of intersections of dislocation lines, L is the total lines of all the dislocation lines, t is the TEM specimen thickness. For as-built bcc iron, the dislocation density measured by XRD techniques is about 1.8×10^{15} m^{-2} [84], while by TEM observation, the value will turn to 2.33×10^{14} m^{-2} [85]. Notice these two methods only provides estimated result. Further development is required.

The well-known Hall-Petch equation describes the grain boundary strengthening σ_{gb}. Smaller the grain size, higher the strength. How to define the grain boundary is a problem sometimes. In reference [86], the grain boundaries with a misorientation angles greater than 2° have the same strengthening effect as conventional ones. I boundaries with a misorientation lower than 2° can be treated as an array of dislocations and contribute to dislocation strengthening. The contribution from the grain boundary strengthening σ_{gb} can be expressed as modified Hall-Petch equation (19) [87]:

$$\sigma_{gb} = \frac{k_{HP}}{\sqrt{d_g}} \tag{19}$$

where k_{HP} is a constant and can be taken as 210 Mpa·$\mu m^{1/2}$ for bcc iron [86], d_g is the average grain size in μm.

When solid solution is formed, alloying elements dissolve into base metal to form a solid solution. Solid solution strengthening effect can be evaluated by the Fleischer equation (20) [87]:

$$\sigma_{ss} = (\textstyle\sum_i \beta_i^2 c_i)^{1/2} \tag{20}$$

where β_i is the strengthening constant of element i, and c_i is the atomic fraction of element i in matrix. As can be seen, the solid solution strengthening is the integrated contributions from each element. The β_i of each element is determined by the shear modulus and the lattice misfit caused by this solute element. For certain solid solution, β_i increases with the difference of atomic size between solute and solvent. For example, Cu contributes little to solid solution strengthening in bcc Fe matrix due to small difference in atomic size. The corresponding β_i is about 320 for Cu. The β_i for Mo atom is as large as 2143 due to the much larger atom size difference. On the other side, if the atoms are small enough (such as C atoms), these atoms could be interstitial atoms and provide a large strengthening effect. The strengthening constant of some elements in bcc Fe matrix is given in Table 3 [84][88][89].

Table 3. The solid solution constants in bcc Fe matrix.

Elements	C	Ni	Mn	Si	Mo	Cu	Cr	V	Ti
β_i	2887	334	213	732	2143	320	434	404	2628

The last contribution to material strength is the intrinsic strength of the base element σ_0. For bcc Fe, the value is about 50 MPa [84]. Equation (21) can be used to predict the yield strength of a material by considering all these strengthening contributions.

$$\sigma_y = \sigma_0 + \sigma_{pcpt} + \sigma_{dis} + \sigma_{gb} + \sigma_{ss} \tag{21}$$

However, the above equation is just a simplified model. The real situation would be more complicated. For instance, precipitation consumes alloy elements, resulting in a reduction of the solid solution strengthening. Also, the precipitates located at different sites (such as matrix, grain boundaries) will lead to different strengthening effect. Meanwhile, the dislocation density may change during that precipitation. All make the prediction more complicated.

Chapter 5 – Wear Mechanisms of Steel

5.1 Introduction to Tribology

The term tribology was first introduced by a British committee in 1966 [90]. The purpose of this action was to improve the understanding of lubrication and reduce the cost during industrial production because people realized that lubrication was more complicated than expected. In many cases, the study of tribology focuses on the interactions between two (sometimes three) bodies sliding against each other. The interactions caused by sliding include friction, wear, friction heat and so on.

Friction is usually defined as the resistance that one surface of a solid object encounters when moving over another. The magnitude of the friction depends on the surface material of the two sliding/rolling objects and the applied load perpendicular to the sliding/rolling plane. It can also be expressed quantitatively as the normal load applied multiplied by the friction coefficient. Depending on the application, friction can be either beneficial or detrimental. In industry, making good use of friction can improve machine efficiency and save natural resources.

Tribology is a multidisciplinary research field involving mechanics, materials, physics, chemistry, metallurgy etc, as verified by a variety of wear mechanisms. Burwell [91] summarized six main forms including abrasive, adhesive, surface fatigue, erosive and fretting, and chemical. In a specific application, the relevant wear mechanism depends on operating conditions such as material, temperature, pressure, humidity, etc. Often, several mechanisms take effect jointly or in sequence.

Wear is defined as the material removal from sliding/rolling objects. The desired wear is the one that can be controlled for some specific purposes, such as machining and polishing, while the undesired wear refers to the unexpected or detrimental results on the component during friction. The wear of materials can be quantitatively characterized by wear rate, which describes the weight or volume of removed material per unit sliding distance or time. The unit can be $mm^3 \cdot Nm^{-1}$, $mm^3 \cdot m^{-1}$, $mg \cdot m^{-1}$, $mg \cdot s^{-1}$, et al. However, the most widely used one is $mm^3 \cdot Nm^{-1}$.

5.2 The Wear of Steels at Room Temperature

When the friction occurs at room temperature, the major wear mechanisms are usually abrasive, although in some cases with high pressure or high frictional heat, adhesion and oxidative wear may also arise simultaneously. However, even just abrasive wear, it is not easy to prevent or control. Because in reality, there always has several different mechanisms of abrasive wear at the same time. Only using the term of abrasive wear cannot precisely describe the wear mechanism.

Micro-cutting, microfracture, fatigue by repeated ploughing, and pull-out of individual grains or hard phase are the main mechanisms of abrasive wear [92]. The first mechanism, micro-cutting, usually occurs when the abraded material is soft. The sharp grit or hard asperity cut the soft material and removes it in the form of debris. This is the classic model for abrasive wear.

The second one, microfracture, applies when abraded material is brittle. Grit breaks the abraded material into fractured particles. When the local surface is repeatedly ploughed and deformed by grits; some materials will be detached due to metal fatigue. This is the third mechanism, fatigue. The fourth one, pull-out mechanism, usually applies to materials containing ceramics or hard phase particles. When meeting grit, hard phase particles, the hard particles may be scraped out from the material due to the relatively weak bonding between particles and matrix.

For steels, micro-cutting and fatigue are common wear mechanisms, because steels are often ductile. However, when metal is very soft, instead of cutting, grits may push metal forward or to both sides to create a protruding edge. In this case, the material is not removed from the surface. This wear mechanism is named ploughing [93]. For the cutting process, the worn material forms debris in front of the grits and the volume of the debris is equal to the volume of the groove. Ploughing and cutting can be discriminated based on this. However, in many actual situations, the grooves are characterized by both side ridges and cutting debris. This means there is no strict boundary between micro-cutting and micro-ploughing. To some extent, it is acceptable to use the terms interchangeably.

In practice, fatigue and micro-cutting are presented simultaneously. As described above, the ridges or deformed fields can be formed at the sides of the groove during micro-cutting. Fatigue micro-cracks and debris could be generated in these regions after repeated scratching. However, fatigue wear would be a mild or slow wear form for metallic material since formation of debris needs repeated deformation.

5.3 The Wear of Steels at High Temperatures

Compared with room temperature, adhesive and oxidative wear plays a more important role at high temperatures. Oxidative wear is easy to be understood because increasing temperature will inevitably accelerate metal oxidation. Adhesive wear can be interpreted from the fundamental of adhesion.

When the distance between two metallic objects is small enough (typically less than 1 nm), electrons can transfer from one object to another and establish metallic bonds [92]. Strong metal-to-metal bonding force is achieved. However, in general, there are very few such contact area between objects, so the adhesive force formed is not high, especially for the materials with high hardness and elastic modulus. For metals with good ductility, the real contact area can be increased by plastic deformation, which will improve the adhesive force between metal bodies. Similarly, the increase in temperature can generally significantly improve the ductility of metal materials, which will also enhance the adhesive force during the friction process.

Despite of the strong adhesion force at the atomic level, the tendency to adhere is variable when the contacted solids have different compositions and crystal structures. In general, the adhesion force between similar materials is large, such as bcc-iron to bcc-iron. The relatively low adhesive force between different crystals is due to the high degree of lattice mismatch at the bonding surface. In addition, it has also been found that the adhesion tendency of the solid with the close-packed hexagonal (hcp) crystal is significantly lower than that of bcc or fcc [94]. This is due to the fact that hcp crystal has fewer slip systems, and thus higher modulus of elasticity and higher hardness, which result in lower adhesion force. From another aspect, Song [95] et al. reported that the adhesion force between two materials is related to their interfacial energy. The simulation performed in that study shows that when interfacial energy is small, substantial plastic deformation occurs on the separation of the two sticked parts, and some of the material originally in the asperity is transferred to the opposing substrate. When the interfacial energy is large, the separation of two materials occurs at a well-defined critical force, with no material transfer and no plastic deformation. Although this conclusion is drawn by simulation, it is still consistent with the discussion on the adhesion force at the start of this paragraph. In addition, metals with high chemical activity also exhibit strong adhesion force. However, on the other hand, metals with high chemical activity are easy to be oxidized at high temperatures, and the oxide film can prevent real contact between metals and thus hinder the adhesion. The situation becomes complicated.

Under the conditions of high temperature and stress, the mechanism of adhesive wear is somewhat similar to that of welding. The adhesion force between two objects is at the atomic level and is very high. Adhesive wear is therefore a critical and challenging issue in hot stamping.

The oxidative wear of the metal will be greatly increased when the temperature rises, typically higher than 0.4 T_m in Kevin. High-temperature exposure leads to thicker oxide layers and more oxide wear debris. With the combination of higher pressure, these oxide wear particles can be compacted into a solid "glaze" layer which is usually constituted by a mixture of oxides and base metal instead of pure oxides. After being subjected to severe deformation, the microstructure of the "glaze" layer can be very fine, even nanostructured. The formation of a "glaze" layer may significantly decrease the wear rate. Therefore, some materials show relatively low wear rates at elevated temperatures than that at room temperature. Staia et al. [96] examined the wear resistance of D2 tool steel at room temperature, 300 ℃ and 600 ℃. The results showed that the largest wear is at 300 ℃, while the lowest is at 600 ℃ which is even lower than that at room temperatures owing to the formation of the protective glaze layer.

However, the “glaze” layer could develop into a cumulative form. Macroscopically, this form is manifested as galling. During the service of hot stamping, galling on tool steel is a detrimental behavior. It will scratch the blank workpiece. Moreover, the protrusion of galling can create a gap between tool steel and the workpiece, which will influence the heat transfer from the workpiece to the tool and decrease the cooling rate of the formed workpiece. The strength of the workpiece then cannot reach the level demanded. Hence, galling should be avoided as much as possible during the hot stamping process.

Oxidative wear can also be aggravated by the delamination and cracking of oxide layer. Delamination can be caused by the volume changing of oxide. Usually, the volume of oxide is different from the volume of the metal. Pilling–Bedworth ratio (P–B ratio) is defined as the volume ratio of the oxides to the corresponding metal [97]. When it is less than 1, the formed oxide layer will shrink and form a porous structure. When the P-B ratio is greater than 1 and less than 2, the oxide layer could be dense. When it is greater than 2, the oxide film will be over-expanded and peeled off. For iron-based materials, the P-B ratios of the oxidation products are 2.14 for Fe_2O_3 and 1.90 for Fe_3O_4, respectively [98], implying a risk of oxide spalling. Moreover, due to the large contact stress (both normal stress and shear stress), the oxide layer can be fractured during the hot stamping process, which can again increase the risk of the spalling of the oxide layer and further oxidation of the fresh material.

However, it is still a debate whether the oxidative debris contributes to abrasive wear on iron-based materials or not. Although Fe_2O_3 has high hardness, Fe_3O_4 and FeO have low hardness but better ductility. In the reality, the oxidative debris is usually a mixture of oxides (may contain metal). It is hard to tell which constituent dominates the wear behavior. Furthermore, the softening of the matrix material at high temperatures also influences the wear behavior, which makes it complicated and difficult to evaluate the impact of oxidative debris on abrasive wear.

Chapter 6 – Experimental Methods

6.1 Materials and Metallographic Sample Preparation

6.1.1 Modified H13 Hot Working Tool Steel

The nominal composition of the alloy is X32CrMoNiW3-2. It was modified based on H13 tool steel (M-H13) to optimize the properties at elevated temperatures for the intended applications. In this study, parts were produced by L-PBF using gas atomized powders supplied by Uddeholms AB. The particle size of the powders is in the range of 20 to 50 μm. For the microstructure characterization, samples were prepared by following standard Struers metallographic procedure and then etched with the etchant of 5% picric acid + 1% HCl + 94% ethanol for 30 seconds.

6.1.2 Tool Steels for Hardfacing

Three pre-alloyed tool steel powders supplied by Uddeholms AB were used as feedstock material for DED and, process. They are gas atomized Vanadis 4 Extra SuperClean (V4E, a cold work tool steel), a high boron steel grade (HBS, X50MoCoCr17-4, a ceramic phase strengthened tool steel) and a newly developed maraging steel (NMS). The chemical compositions of V4E, NMS and substrate are shown in Table 4. The substrate is Dievar hot work tool steel in a size of 117 × 59 × 25 mm^3, supplied by Uddeholms AB as well. The powders in the particle size between 45 μm to 150 μm were cladded on the substrate in the form of 1-layer, 2-layers, and 4 (8 for NMS) -layers. For the microstructure characterization, samples were etched using the same etchant as given in 6.1.1.

Table 4. Nominal chemical composition of the tool steels provided by the powder suppliers in wt.%.

	C	**Si**	**Mn**	**Cr**	**Mo**	**V**	**Co**	**Ni**	**Cu**	**Fe**
V4E	1.4	0.4	0.4	4.7	3.5	3.7	-	-	-	Bal.
NMS	0.03	0.35	0.4	5.0	8.0	-	12	2.0	2.0	Bal.
Dievar (Base material)	0.35	0.2	0.5	5	2.3	0.6	-	-	-	Bal.

6.1.3 Laser Powder Bed Fusion

Cubes of M-H13 steel in the size of 10 × 10 × 10 mm^3 were produced by L-PBF method using SLM 125 HL system (SLM solutions Group AG) equipped with a YAG laser of maximum power of 400 W. The laser had a power of 175 W and a beam diameter of 65 μm. The building chamber was filled with inert argon gas (12 mbar inside pressure). The preheating temperature of the baseplate was 200 ℃. The scanning speed was 720 mm/s and hatch spacing between tracks was about 120 μm. The layer thickness was chosen to be 30 μm.

6.1.4 DED Process

For the materials applied for hardfacing, their powders were cladded on the Dievar substrate by DED method. The DED system was combined with a 5-axis DED Laser printing machine with a YAG laser of maximal power of 4000 W. The laser power applied in this study was

1600 W. The shielding gas used to carry powder and protect melt pool was argon inert gas. Before the cladding, the baseplate wasn’t preheated. The scanning speed was 520 mm/min and the hatch spacing between tracks was 1.8 mm. The layer thickness was designated to 1.6 mm. A zigzag scanning pattern was applied in the cladding process. For the 1-layer and 2-layers specimen, the cladding area was 102 × 52 mm^2, and for the 4-layers specimen, the cladding area was changed to 48 × 50 mm^2.

6.1.5 Post Heat Treatment

After L-PBF, selected M-H13 steel samples were divided into two groups. The samples in the first group were treated at 1020 ℃ for 30 min followed by quenching in oil and subsequently tempering twice at 580 ℃ for 2 h. The samples in the second group were directly tempered at 625 ℃ for 2 h to reduce the retained austenite and to relieve the stress. Selected samples from these two groups were treated subsequently at 550 ℃ and 600 ℃ for 5 – 100 h followed by air cooling to evaluate the softening behavior at elevated temperatures.

After DED, the optimization of tempering parameters was carried out on the cladded tool steels. The parameters varied were temperature levels (525, 535 and 550 ℃) and tempering times (2 h for 2 times, 2 h for 3 times and 3 h for 2 times). The best tempering parameter was defined when the highest hardness was obtained. Using this method, the best tempering parameter determined was 2 h for 2 times at 525 ℃ for HBS, 2 h for 3 times at 550 ℃ for V4E, and 3 h for 2 times at 535 ℃ for NMS, respectively. The softening resistance of such tempered steels was also examined in terms of room hardness and wear resistance by means of two approaches. One was time dependent softening treatments at 550 ℃ and 600 ℃ for 5 – 100 h. Considering the temperature of the hot workpiece during hot stamping may reach ~ 800 ℃, another approach was temperature dependent treatments at 600, 700 and 800 ℃ for 3 h.

6.2 Analysis Techniques

6.2.1 Optical Microscopy

A Leitz DM-RZ light optical microscope (OM) with Axiovision 4.8 software and a Zeiss Axioscope 7 light optical microscope with Zen Core 2.7 software were used for imaging the microstructure on polished and etched sample surfaces. Integration function provided by Zen Core 2.7 software was used sometimes to stitch the images to obtain a large field of view. With the help of ImageJ software, the relative density of the printed samples can be measured. As shown in Figure 12, the region of the cladded layer is first extracted from the overview image on the cross section (a). Subsequently it was converted into 8-bit grayscale (Figure 12b) in order to separate the feature with different contrast. Adjusting the upper and lower threshold properly can highlight the edge of the features of interest which is defects in this case (Figure 12c). Last, the thresholded pixels were set to black and all other pixels to white (Figure 12d), by which the area fraction of the defects in this image can be measured and relative density can be estimated. Notice non-porosity defects (e.g., cracks) were included. The relative density value is averaged from 8 stitched images.

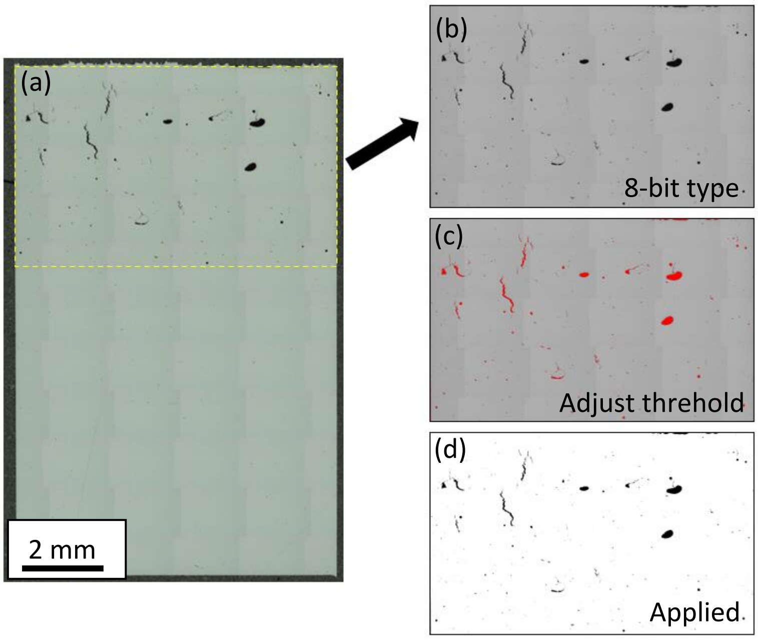

Figure 12. The process of relative density measurement for cladded V4E layer from OM images using ImageJ software.

6.2.2 X-ray Diffraction

If monochromatic X-rays is radiated at a crystalline material, one observes diffraction of X-rays at various angles. X-rays generated from a given anode material have a constant wavelength. The commonly used anode materials are Cu and Cr. The relationship between the X-ray wavelength, λ, the angle of diffraction, 2θ, and interplanar spacing of the crystal lattice, d, is given by Bragg's law in Equation (22):

$$n\lambda = 2d \sin\theta \tag{22}$$

where n represents the order of diffraction. The diffraction occurs only for some specific interplanar spacing. In a Bragg-Brentano geometry, the incident angle and the diffraction angle vary simultaneously. The primary phases in metallic samples can be identified by X-ray diffraction (XRD) through analyzing their lattice structure. In the present study, Bruker AXS D8 Advance diffractometer equipped with Cr K_α radiation is used. Prior to the measurement, the samples were ground and polished following the standard Struers metallographic procedure.

6.2.3 Scanning Electron Microscopy

Scanning electron microscopy (SEM) is a versatile equipment as it can provide various information depending on the user's demand. As its name implies, an electron beam is used to scan the specimen surface. Various types of signals are generated when the electron beam is interacting with the specimen, such as secondary electrons (SEs), backscattered electrons (BSEs), characteristic X-rays and auger elections. These signals are subsequently detected by appropriate detectors. Making a good use of these signals can result in highly useful information about the materials.

For example, SEs originating from the atoms at the near-surface regions of the specimen, can give the topographic information of specimen's surface. SEs are a result of inelastic interaction between primary electron beam and the surface atoms of the specimens. The interaction volume of SEs is relatively small compared to BSEs and X-rays, as shown in Figure 13. Although the interaction depth of electron beam and specimen can reach a magnitude of micrometers, only the electrons originating from a depth less than 10 nm can escape and be captured by the detector [99]. This shallow depth of SEs makes them suitable for depicting the topography. SEM in this mode usually has a high resolution, typically ~10 nm.

Different from SEs, BSEs essentially are the primary electrons. They are from elastic scattering between the atoms from the sample and the electron beam. After the interaction, there is no energy loss compared with the primary electron. With this high energy, the generation volume of BSEs is larger than that of SEs, about several tens of nm. Hence, the mode of BSEs can also give the information of topography but has a poorer resolution than SEs. Since large atoms have a stronger ability of scattering electrons than light atoms. Therefore, a stronger signal can be captured in the region with high atomic numbers. BSEs signal can provide composition contrast and help us distinguish different phases.

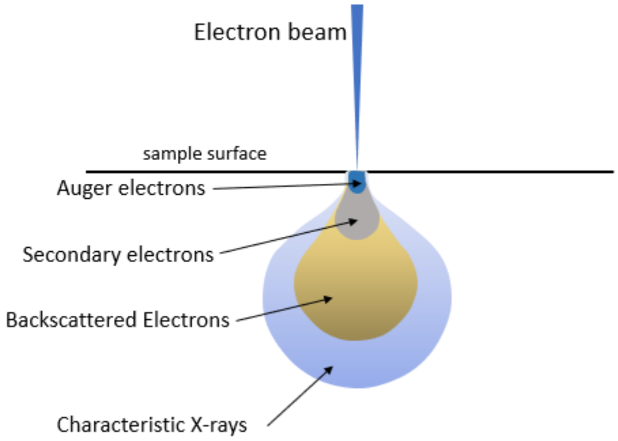

Figure 13. Schematic of the interaction between electron beam and material.

There are also characteristic X-ray and Auger electrons besides BSEs and SEs. Auger electron spectroscopy will be discussed in Section 6.2.4. When electron beam strikes on specimen surface, some atoms will release their inner shell electrons and leave a vacancy there. It is an unstable state. If the outer shell electron migrates and fills that vacancy, X-rays could be emitted due to the higher energy of the outer shell electron. The differences in energy between specific outer shells and inner shells are characteristic. Hence, the emitted X-rays are also characteristic. The chemical composition of specimens can be obtained by considering the energy and counts of these X-rays. This is the principle of energy dispersive X-ray spectroscopy (EDX or EDS) technique equipped on SEM instrument. The special resolution of EDX depends on the sample material and beam energy but is usually in the order of ~1 μm.

6.2.4 Auger Electron Spectroscopy

As depicted before, when a specimen is probed by an electron beam, inner shell electrons could be ejected and the outer shell electron, which is at a high energy level, migrates to the inner shell. Due to the conservation of energy, the excess energy will be released by either a characteristic X-ray or exciting another outer shell electron to escape from the atom. This “escaped” electron is termed the Auger electron, as shown in Figure 14. Moreover, the kinetic energy of Auger electron can be calculated approximately by the energy of the core hole (E_k) and the energy level of two outer electrons (E_{L1} and E_{L2}), as expressed by Equation (23):

$$E_{KL_1L_2} \approx E_K - E_{L_2} - E_{L_1} \tag{23}$$

where $E_{KL_1L_2}$ is the kinetic energy of a KL_1L_2 Auger electron, E_{L_2} and E_{L_1} are the binding energies of two outer electrons respectively. The terms of $E_K - E_{L_2}$ is the difference in energy of migrated electron before and after transition. It is worth to notice that this equation does not consider the interaction energy between the holes on L_1 and L_2 level in final state nor the atomic relaxation energy and extra-atomic relaxation energy. However, it expresses the mechanism of auger electron emission.

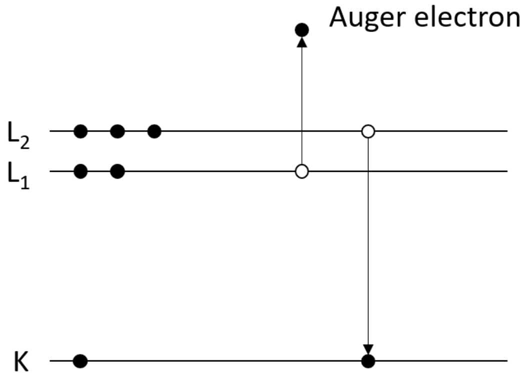

Figure 14. Schematic of Auger electron.

From Equation (23), it is known that the kinetic energy of Auger electron is not related to the energy of the primary electron beam. These characteristic kinetic energies can be used to identify the elements at the surface. The intensity at specific kinetic energy can be used for semi-quantification of the composition. Due to the low energy of Auger electrons, the escape depth is in a range of 0.5 – 8 nm. Hence, Auger electron spectroscopy (AES) is a surface sensitive technique and offers the capacity to analyse surface chemical composition with high lateral resolution. This is different from EDX. In the present study, a PHI700 instrument from Physical Electronics with lateral resolution of ~ 10 nm was used.

6.2.5 Transmission Electron Microscopy

As discussed in the section of SEM, various signals can be obtained when an electron beam radiates on a specimen. If the specimen is thin enough (typically less than 100 nm), the transmitted electron can penetrate through the specimen. This is the fundamental principle of TEM. The primary electrons are generated from an electron gun equipped with a tungsten filament or a single crystal LaB$_6$ filament. These electrons are subsequently accelerated to high energy (typically 80 – 300 KeV) and then focused into a small probe by a set of magnetic lenses. The focused beam can be transmitted through the thin film sample and forms high-resolution images on a fluorescent screen, as shown in Figure 15. Theoretically, the resolution of the images depends on the wavelength of the electrons. Higher the energy, shorter the wavelength of the electrons. The wavelength of the electrons λ can be expressed as following Equation (24):

$$\lambda = \frac{h}{\sqrt{2em_0U(1+\frac{eU}{2m_0c^2})}} \tag{24}$$

where h is the Planck's constant, U is the accelerating voltage used, c is the speed of light, e and m_0 are the charge and mass of the electron. For example, if the accelerating voltage used is 200 keV, the corresponding wavelength of the electron is about 0.025 Å, which is lower than the diameter of an atom by two orders of magnitude. Hence, the images formed by these transmitted electrons have the capacity of showing fine details and even an arrangement of atoms.

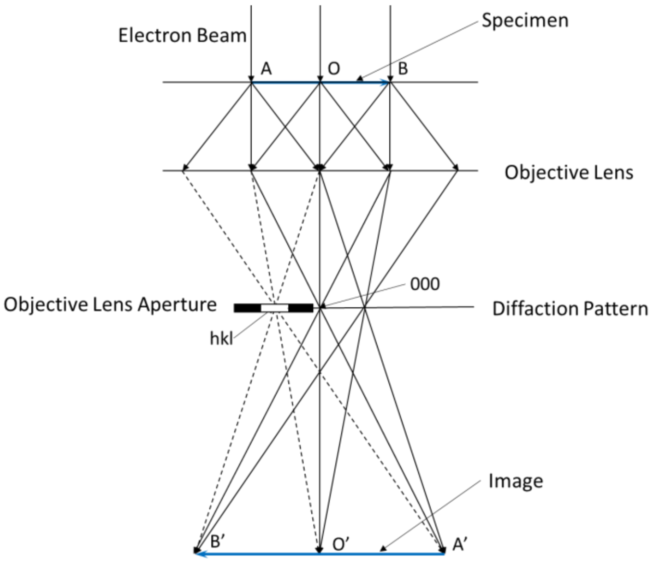

Figure 15. The schematic diagram of transmission electron microscopy. The dash lines indicate the mechanism of dark field imaging.

Apart from the conventional imaging function, TEM also has the modes of selected area electron diffraction (SAED). As we know, electrons have both wave and particle properties. When the electrons transmit the specimen, the lattice structure in the specimen can be considered as a raster. The electrons will be diffracted by the periodically arranged atoms to specific spots. A diffraction pattern can then be generated at the back focal plane on the magnetic lens as shown in Figure 15. SAED pattern can provide the lattice structure and orientation information of the lattice structure. Based on this, the dark field image can also be provided. As indicated by the dash lines in Figure 15, inserting the objective lens aperture to a certain spot can form a dark field image. The dark field image can be used to examine the regions that contribute to a specific spot in SAED pattern. Moreover, energy-dispersive X-ray spectroscopy and convergent beam electron diffraction (CBED) can be performed on TEM as well. In a word, transmission electron microscopy (TEM) is a powerful technique for microstructure analysis, phase identification and compositional investigation, especially for nanoscale features. The TEM instrument used in the present study is a FEI Tecnai T20 LaB6 microscope operated at 200 KV equipped with an Orius 200 CCD camera.

6.2.6 Simulation Software

Simulation by means of ThermoCalc and JmatPro can efficiently predict the microstructure, phases and properties of target materials. Software ThermoCalc 2019a with the access to TCFE10 database was used in this study. Based on the composition and temperature, many properties can be simulated such as thermophysical properties (e.g., density, coefficient of thermal expansion, viscosity), kinetic properties (e.g., diffusion coefficients, atomic mobility), characteristics related to equilibrium and non-equilibrium solidification (e.g., freezing range, shrinkage) using different databases and theoretical models. In this study, solidification, specifically, solid fraction of specific steels was calculated under both equilibrium and non-equilibrium conditions by Scheil solidification simulation. Another simulation software, JmatPro v.11, was used to predict CCT & TTT diagrams and to simulate the precipitation behavior during the steel tempering.

6.2.7 Mechanical Testing

Tensile testing. After the designed heat treatment (as shown in Section 6.1.5), the specimens of M-H13 steel produced by L-PBF were post machining to prepare cylindrical tensile bars with thread-end and a gauge length of 25 mm and a diameter of 5 mm. Testing was performed on an Instron 4505-5500R tensile tester with strain rates of 10^{-4} s^{-1} and 10^{-1} s^{-1} in order to investigate the tensile behavior including strain rate sensitivity of AM parts under different conditions. The obtained engineering stress-strain data were converted into true stress-strain data by Equations (25) and (26):

$$\sigma_t = \sigma(1 + \varepsilon) \tag{25}$$

$$\varepsilon_t = \ln(1 + \varepsilon) \tag{26}$$

where σ and ε is the engineering stress and strain while $\sigma_t$and ε_t are true stress and strain, respectively. These two equations are not valid after necking.

Impact toughness testing. The energy absorbed by the specimen upon fracture can be used to evaluate the toughness of the materials. Charpy V impact toughness test is a popular method to evaluate the toughness in materials science and metallurgy due to its simple sample preparation and quick supply of the result. During the test, a pendulum at a fixed known height is released down and strikes the specimen at the lowest position. By measuring the angle of the pendulum at the rest travel, the energy absorbed by the broken specimen can be calculated. In the present study, the specimens have a dimension of 55×10×10 mm^3. The V notch located at the longitudinal side was 2 mm deep with a 45° angle and a tip radius of 0.25 mm. The tests were carried out on a Roell Amsler RKP instrument. The energy of the pendulum was preset to 150 J.

Hardness testing. Hardness is the ability of materials to resist local plastic deformation. It is a critical mechanical property for tool steels. In this study, Vickers hardness (HV) test was performed by means of a DuraScan 70-G5 instrument with the ASTM E384-17 standard. During the test, a pyramidal diamond indenter was pressed into the specimen with a chosen load (10 kg for macro hardness and 0.1 kg for micro hardness in this thesis) to form a square indentation. Then the hardness (HV in kgf/mm^2) was calculated by Equation (27) using the average diagonal length *d* measured from the indentation.

$$HV \approx \frac{1{,}8544F}{d^2} \tag{27}$$

Every hardness value is the average of more than 6 measurements in this study [100].

6.2.8 Abrasive Wear Testing.

The samples for the abrasive wear test were shaped into cylinder geometry with 12 mm in diameter and 20 mm in height. Before the test, the top surface of the samples was machined into a flat plane by using an industrial planar grinding machine. The abrasive wear tests were carried out on a steel wheel abrasive test machine. The machine was a modified type from a grinding machine (ASTM G65 standard). In the test, the steel samples were under a normal load of 17.8 N against an aluminum oxide sandpaper with a particle size of P800. The sandpaper was renewed every 15 s. The total testing time for each sample was 60 s. During the test, the sandpaper was welted by a water flow of 1.5 L/min. After the test, the weight reductions of dry samples were recorded by an electronic balance. Wear resistance was assessed by the weight reduction in mg/min.

Chapter 7 – Summary of Results

This chapter is a summary of the studies done within the framework of this thesis. The detailed work and discussion are presented in the appended papers. This section includes four parts. The first part addresses the research motivation of the thesis. A case study was performed on a failure mold from a hot stamping process in order to gain information of the failure mode. It pointed out a combined failure mechanism including adhesive wear, surface softening and the spalling of delaminated white layer. In order to meet the challenges faced by hot work tool steels, two AM techniques including L-PBF and DED were adopted to fabricate a few selected tool steels. In the second part, a modified H13 hot work tool steel was fabricated by L-PBF. The effect of two types of post heat treatment on mechanical properties and softening resistance was characterized and discussed. In the third part, three types of tool steels were deposited for the hardfacing purpose by means of DED. Firstly, defects were investigated on the as-deposited samples, especially for V4E steel. Then, softening resistance of the three steels were assessed by two strategies, i.e., either at fixed temperature with varied softening time or at varied temperature with a fixed time. Abrasive wear resistance of as tempered and softened tool steels manufactured by DED was also evaluated. Comparison of softening resistance and wear resistance between conventional and additively manufactured tool steels was performed as well.

7.1 The Failure Mechanism of a Hot Stamping Mold

In **Paper I**, an investigation was performed on a worn die (Uddeholm QRO 90 Supreme tool steel) used for the hot forming of uncoated boron steel sheets. The surface and cross-sections have been studied with a focus on the origins and the evolution of various wear phenomena during the hot stamping process. An insight into the wear situation that the dies underwent and a potential solution for the failure of hot stamping dies was provided.

Hardness measurements of the sub-surface on the cross-section at the round corner revealed the softening of QRO 90 tool steel during the hot stamping process, as shown in Figure 16a. As we can see, the hardness of the sub-surface was significantly lower than that of the bulk (~570 HV). The softening of the sub-surface was believed to be related to the heating effect from the hot workpieces. As shown in Figure 16a, the softening phenomenon became weaker and weaker from the entrance (Site 1) to the exit (Site 6) of the round corner. Moreover, the softening depth of the sub-surface also decreased from ~ 250 μm to ~ 150 μm. This could be explained by the decrease in temperature when the boron steel workpieces travelled from the entrance to the exit of the round corner. A softened die surface could be scratched by hardened workpiece and presents a rough surface with valley and protrusion, the latter of which could be the initial places for material transfer in the next cycle of forming when the workpiece is hot and soft. Figure 16b shows the transfer material adjacent to the groove on the round corner. Extremely low concentrations of Cr and Mo and a high concentration of O and Mn given by EDS analysis indicate it is oxide of transfer material, which could easily develop into galling. The grooves observed in this figure is the evidence of abrasive wear.

Material transfer was also found on the flat part of the die. As shown in Figure 17, the observation from the longitudinal cross-section shows that there is a layered structure on the protrusion consisting of boron steel layers (e.g., site 4 in Figure 17b) and its oxide layers (site 5 in Figure 17b). It clearly confirms that the galling is formed in a manner of accumulated layers of transfer material and its oxide.

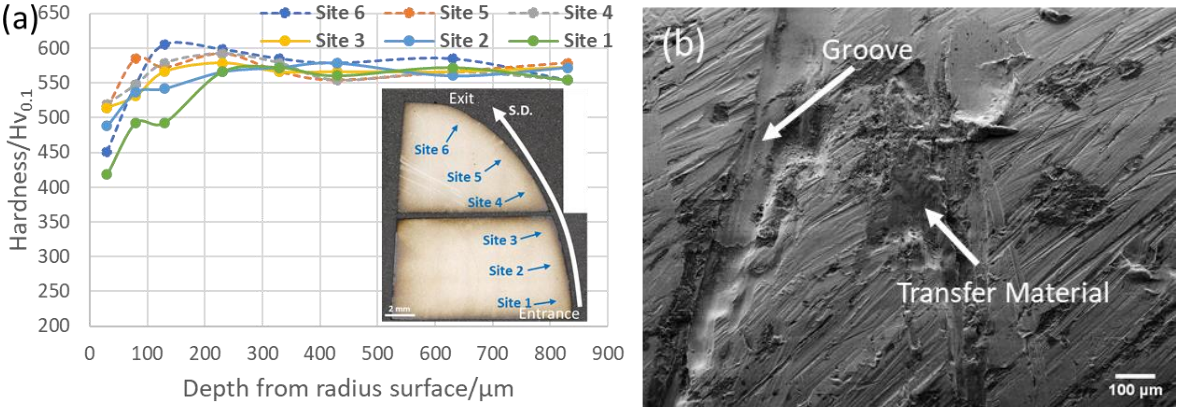

Figure 16. (a) The hardness on the cross section of the round corner of the die (QRO 90 steel) showing the softening of the sub-surface, (b) material transfer observed on the round corner.

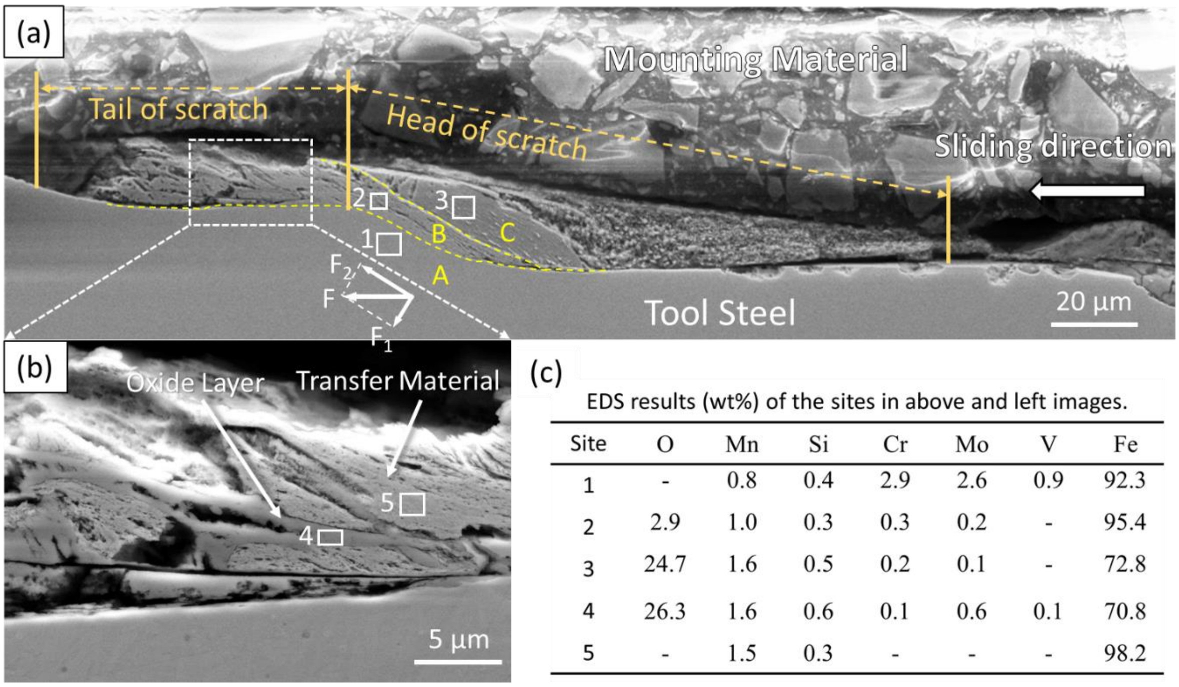

EDS results (wt%) of the sites in above and left images.

Site	O	Mn	Si	Cr	Mo	V	Fe
1	-	0.8	0.4	2.9	2.6	0.9	92.3
2	2.9	1.0	0.3	0.3	0.2	-	95.4
3	24.7	1.6	0.5	0.2	0.1	-	72.8
4	26.3	1.6	0.6	0.1	0.6	0.1	70.8
5	-	1.5	0.3	-	-	-	98.2

Figure 17. (a) SEM image from the longitudinal cross-section (parallel to the sliding direction) of the flat part, (b) Magnified image presenting transferred material in a multilayer form, (c) The corresponding EDS analysis results.

Moreover, a white layer with a thickness of 1 – 2 μm was observed on the surface of the round corner of the die, as shown in Figure 18. Delamination was frequently found between the white layer and substrate. The formation of the white layer and delamination is due to the repeated heating and quenching during the hot stamping process. The spalling of the white layer is considered to be one of the major wear mechanisms of the investigated die. More detailed observation and discussion are presented in **Paper I**.

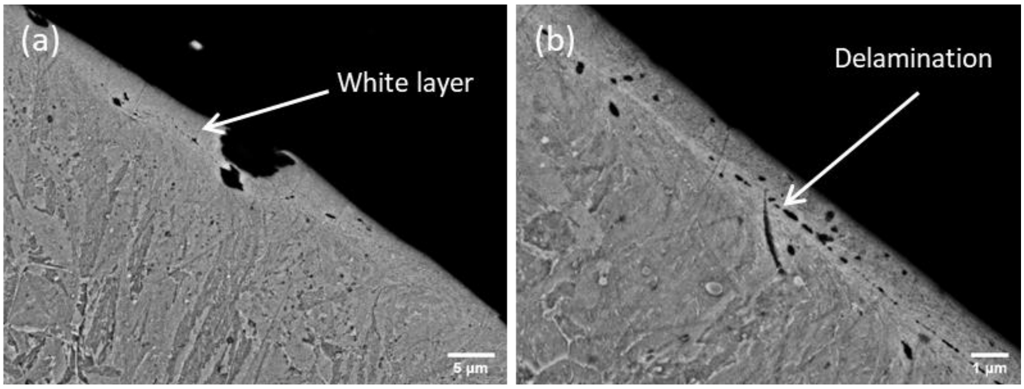

Figure 18. Back scattered SEM images from the cross-section of the round corner center, (a) fractured "white" layer, and (b) delamination below the white layer.

In summary, galling caused by the surface softening and the delamination of the white layer are the primary wear mechanisms for the tool steel investigated. Abrasive wear is observed but is relatively less significant.

7.2 Modified H13 Tool Steel Manufactured by L-PBF

7.2.1 Effect of Post Heat Treatments on Mechanical Properties of M-H13

In **Paper II**, the modified H13 tool steel was printed by the L-PBF technique. The build was crack-free, and porosity defects were rarely found in as-printed samples. The relative density (measured by ImageJ software) of the as-built M-H13 parts is as high as 99.94 %, which means that the built are near-full dense. Melt pool boundaries and cellular structure are observed in the as-printed M-H13 steel. After direct tempering (DT), the boundaries remain but are less clear and the cellular structure in the size range of ~1 μm is maintained (Figure 19a). In the sample with quenching and tempering QT, pool boundaries and cellular structure disappear, and a more homogeneous microstructure of lath tempered martensite is obtained (Figure 19b).

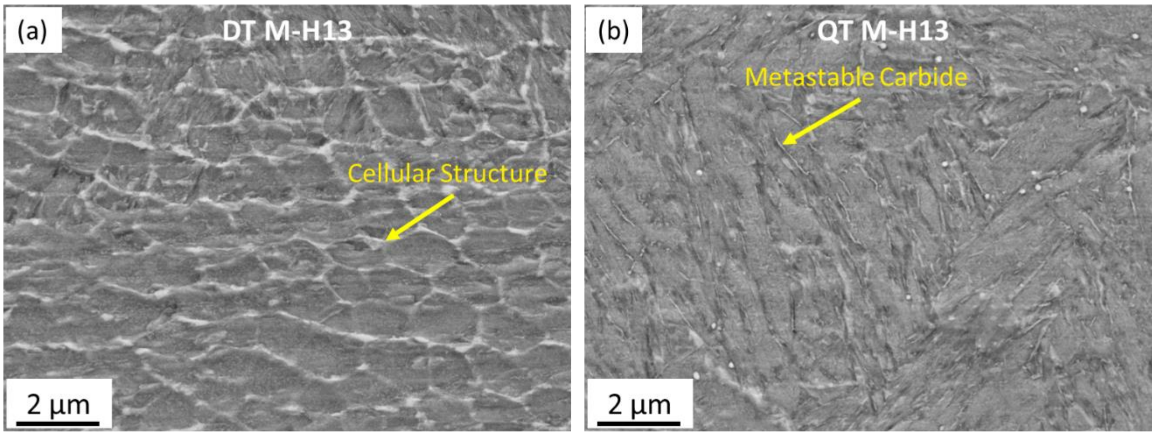

Figure 19. SEM images showing the microstructure of LB-PBF M-H13 tool steel under different heat treatments: a) DT state; b) QT state.

Tensile tests were conducted on the post heat-treated samples. The obtained yield and tensile strength are at levels of ~ 1500 Mpa and ~ 1700 Mpa combined with ~ 10% elongation. In general, QT treatment leads to a slightly lower tensile strength but marginally better ductility, as given in Table 5. Compared to the standard H13 steels fabricated by L-PBF [4][7][101][102][103], M-H13 steel in the present study achieves a good balance between strength and elongation. It has comparable tensile properties to conventional H13 steel. When the strain rate was increased from 10^{-4} s^{-1} to 10^{-1} s^{-1}, the strength of the samples under both conditions increased slightly while elongation remained almost unchanged. In addition, QT samples show a higher strain rate sensitivity (0.00767) than that of DT samples (0.00475), as shown in Table 5, meaning the stronger effect of strain rate hardening. The work hardening capability of QT sample is also higher, as indicated by the strain hardening exponent in Table 5. These two facts explain the significantly higher impact toughness of the QT samples (16.9 J) than that of DT samples (6.5 J).

Table 5. The mechanical properties of M-H13 steels under different conditions.

Sample	Strain rate /s^{-1}	$R_{p0.2}$ /Mpa	R_m /Mpa	δ/%	True $R_{p0.2}$/Mpa	True R_m/Mpa	Strain hardening exponent	Strain rate sensitivity
DT	10^{-4}	1568 ± 9	1736 ± 5	9.9 ± 0.4	1532	1820	0.094	0.00475
DT	10^{-1}	1610 ± 7	1745 ± 9	10.3 ± 0.1	1583	1841	0.081	
QT	10^{-4}	1465 ± 14	1688 ± 9	11.0 ± 0.3	1452	1755	0.111	0.00767
QT	10^{-1}	1514 ± 5	1735 ± 5	10.4 ± 0.6	1529	1776	0.111	

The outstanding tensile properties of M-H13 are related to the microstructure developed in these two conditions (DT & QT). For the DT sample, the strength is supposed to be attributed to both tempered martensite and fine cellular microstructure. Tempered martensite could offer high strength and decent ductility. The boundaries of the fine cellular structure are supposed to consist of micro- segregation and dislocation entanglement, acting as the obstacles to hinder the movement of dislocations and therefore improve the mechanical properties of materials. For the QT sample, the strengthening originates from a complex microstructure of tempered martensite with uniformly dispersed fine carbides along the lath boundaries.

7.2.2 Effect of Post Heat Treatments on Softening Resistance of M-H13

An excellent thermal softening resistance (also named as temper back resistance) plays a key role in hot stamping application. After two different post heat treatments (QT and DT), the evolution of hardness is presented in Figure 20. A similar hardness (527 HV_{10}) is obtained after DT and QT treatment and much higher than that of the as-printed sample. Retained austenite phase are removed in both DT and QT samples. Longer time or higher temperature exposure results in a hardness decrease as expected. A rapid decrease of hardness for both DT and QT samples is found at 600 °C in the first 25 h. After exposure at this temperature for 100 h, the hardness decreases dramatically to about 390 HV for the DT sample and 370 HV for the QT samples. For 550 °C, hardness values are still at a moderate level even after longer holding time for both conditions. However, the decrease of hardness is more severe for QT samples.

The hardness for the DT sample decreases merely by 8.5% from 527 HV to 482 HV after 100 h at 550 °C, while the corresponding decrease for the QT sample is 14.0%. For applications where softening resistance determines tool life, DT could be a promising post-AM heat treatment for LB-PBF produced M-H13 tool steel studied.

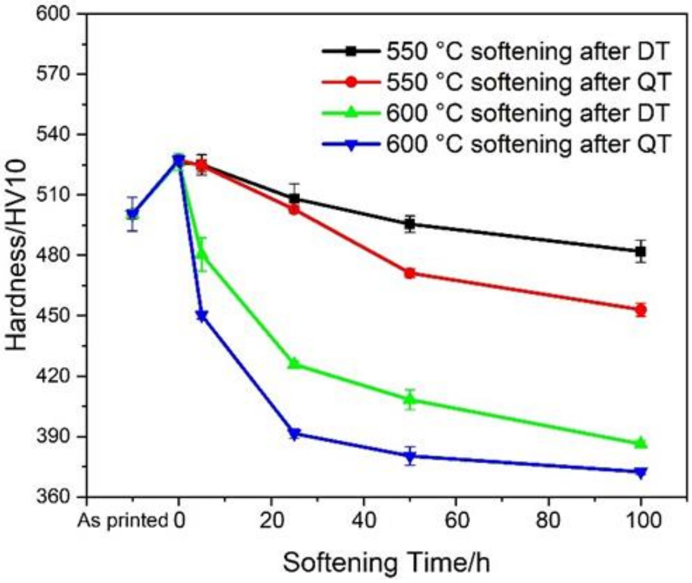

Figure 20. The hardness evolution of L-PBF M-H13 steel at various conditions

The softening mechanisms of DT and QT sample are different. DT samples have a better thermal softening resistance than QT samples, which can be explained as follows. Firstly, cellular structure still exists in the DT sample after isothermal treatment at 550 °C for 100 h, while the metastable M_3C carbides in QT samples are dissolved into the matrix and the hardening effect is therefore lost to some extent. Secondly, M(C, N) particle is critical for softening resistance because it has a much lower coarsening rate than that of Cr-enriched carbides [104]. In DT sample, little V(C, N) was formed during tempering. V(C, N) particles could be precipitated during the softening process, being beneficial to better softening resistance. In QT sample, on the other hand, most of the V(C, N) is formed during the austenitization, which provides less effective hardening. Only a relatively low fraction of secondary V(C, N) will be available during long-term softening treatment. Thirdly, the relatively smaller grain size of ferrite in DT, which can be depicted from full width at half maxima (FWHM) from XRD patterns, is another important reason for its better softening resistance.

Identification of carbides provides a better understanding of the performance of the material. Combined with the simulation of JmatPro and experimental observation, the metastable carbides along the boundaries of lath structure in QT sample were identified as M_3C carbides. During the softening process, the M_3C carbides dissolve into the matrix, and fine Cr-enriched $M_{23}C6$ and V-enriched M(C, N) were formed in the matrix, as shown in Figure 21. Another type of spherical particle in QT sample was confirmed as Mo- and W-enriched M_6C carbides. It was also found in softened DT samples and has been identified by TEM-SAED pattern.

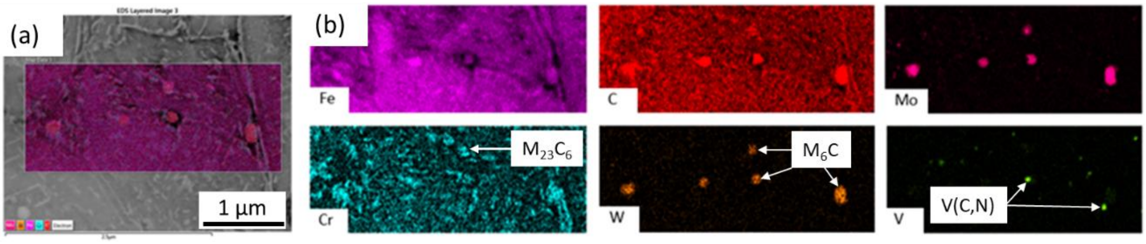

Figure 21. a) SEM image and b) EDS mapping of different carbides in QT+550 °C-100h M-H13.

7.3 Tool Steels Fabricated by DED

7.3.1 Defect Investigation for DED Tool Steels

Owing to the high hardness, unfavorable ductility and high content of the alloying element in tool steels, defects (lack of fusion, pores, and cracks) in AM parts are commonly encountered and challenge the fabrication. In present thesis, three types of tool steels were fabricated by DED, and two of them (HBS and NMS alloy) have a high density above 99.9 % (area fraction). However, V4E samples show a relatively lower density. In **Paper III**, the defects distribution and their formation in V4E have been studied. As shown in Figure 22, cracks and pores were commonly found in the as-deposited sample. Statistical analysis reveals that V4E samples with 1-layer and 2-layers have a similar density of 99.4 % and 99.6%, respectively, while the 4-layer sample has a distinctly lower density of 98.7 %. The defects in 1-layer and 2-layers V4E are mainly pores and some small cracks. However, the 4-layers sample shows significantly more porosity and hot cracking defects in the deposited zone, as shown in Figure 22c.

There are three types of pores in the deposited zone: large irregular pores, keyhole pores and shrinkage pores. The large irregular pores usually have a size above 50 µm and are preferentially located at the interface between layers or at the lower part of the layers. There are two reasons for the formation of this type of porosity. a) Insufficient heat input leads to the short duration of liquid at the near boundary region between different tracks. The liquid there has a lower temperature compared to the central portion and will solidify quickly, which leads to insufficient time for voids to float up. b) formation of a silicon oxide layer on the surface

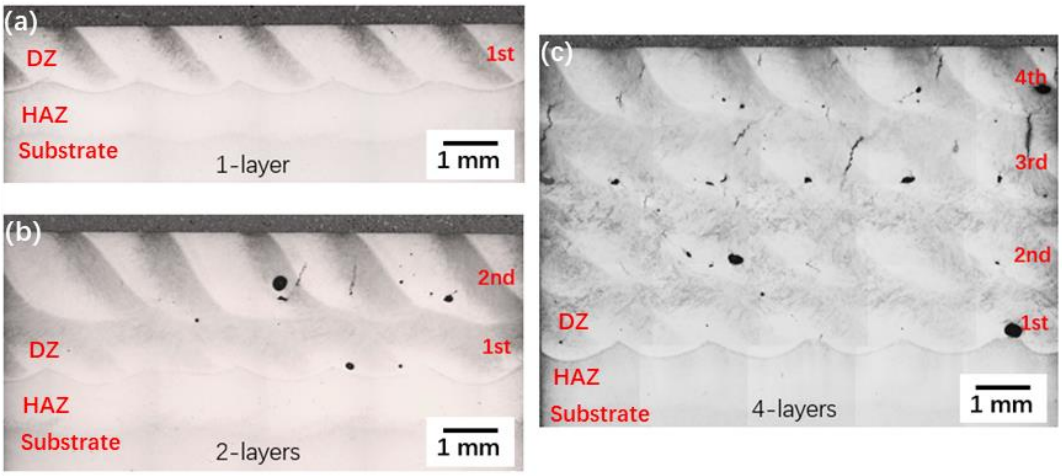

Figure 22. Defects distribution in V4E samples with (a) 1-layer; (b) 2-layer; (c) 4-layer.

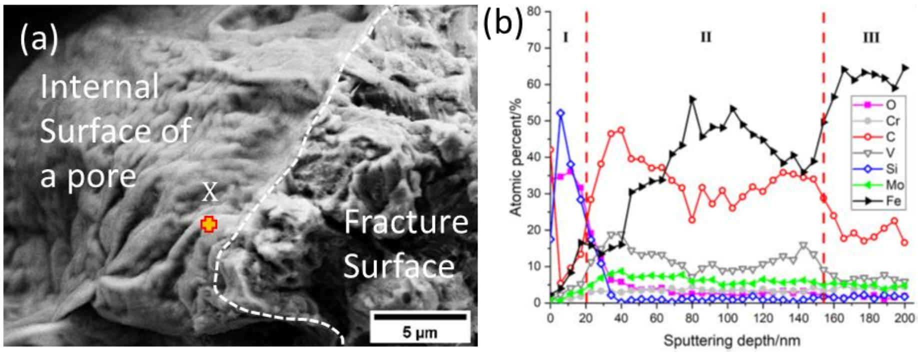

Figure 23. (a) SEM image from fracture surface revealing the internal surface of an irregular pore in V4E steel, (b) AES depth-profiles from point X on the internal surface.

of the irregular pores. The existence of such oxide has been confirmed by EDX mapping, and AES depth-profiling (zone I in Figure 23b. This Si oxide layer may change the surface energy of melt pool and consequently the flow behavior of the melt, preventing the elimination of the pores [105].

Hot cracking has also been frequently found in the upper part of the deposited layers (typically the 3rd and 4th layers, Figure 22). Several factors could influence the formation of hot cracks, such as temperature range of solidification, hardness, build size, and so on. In the present study, V4E steel is a type of high-alloyed cold work tool steel with high strength and hardness. High thermal stress could be introduced during solidification, promoting hot cracking. In addition, V4E has a larger solidification temperature range than that for NMS and HBS from the simulation using Thermo-calc software. This means that the mushy zone will be preserved to

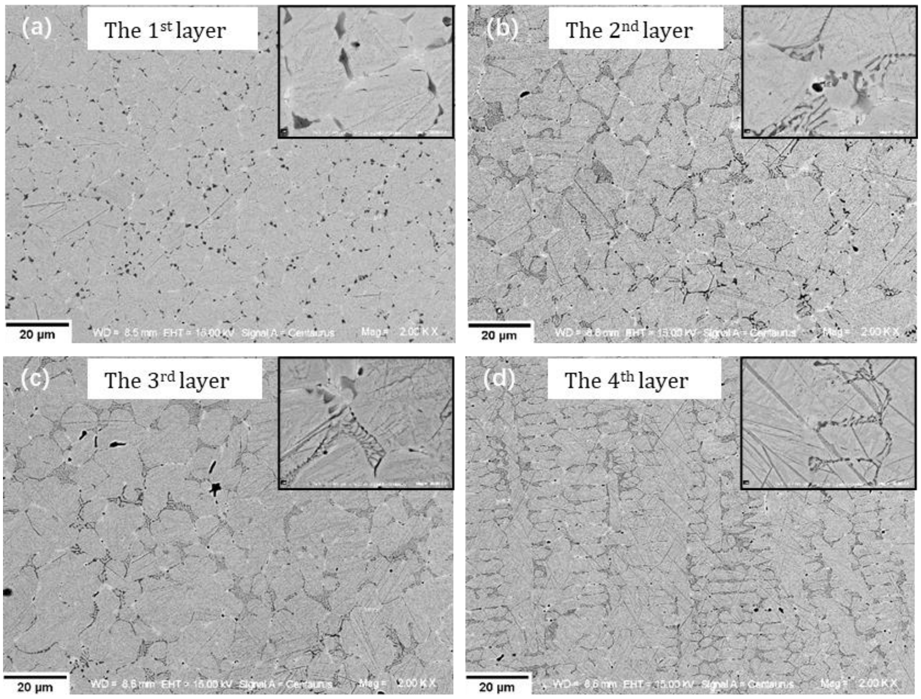

Figure 24. Comparison of the V4E microstructure from different deposited layers: (a) the 1st layer adjacent to the substrate, (b) the 2nd layer, (c) the 3rd layer, (d) the 4th layer (top).

low temperature and promote hot cracking. Moreover, the microstructure of the deposited layers changes from cellular to columnar dendrite with the increase in building height, as shown in Figure 24. The columnar dendrite has a long channel for liquid supply, which could be easily closed by the growth of columnar dendrite. The trapped liquid in the interdendritic region could then form a cavity, leading to cracking. Compared to fine cellular structure, coarser structure and columnar dendrite structure exhibit higher cracking susceptibility. This is an important reason for cracking in the upper deposited layers during solidification.

More discussion about these defects can be seen in **Paper III**.

7.3.2 Time Dependent Softening of Tool Steels by DED

Hot stamping is a high-temperature process which requires that the tools possess high hardness at elevated temperatures. How the hardness of the steels evolutes, when exposed to high temperatures, is of great importance. In order to evaluate their softening resistance, two strategies have been used: (1) Fixed temperature with varied softening time (**Paper IV and V**): 550 and 600 ℃ for 5, 25, 50, and 100 h. (2) Fixed time with varied temperatures (**Paper VI**): 3 h at 600, 700 and 800 ℃. A comparison with the conventional counterparts has also been performed. The time-dependent softening resistance of three tempered tool steels manufactured by DED is focused on in this section. The softening resistance in this thesis is defined as the hardness drop with respect to the as-tempered condition.

NMS alloy is a low-Ni maraging steel with excellent weldability. Defect-free NMS samples were successfully fabricated by the DED technique. No retained or reverted austenite phase can be detected by XRD in both as-cladded and tempered samples. No precipitate but a few primary carbides are found along the prior austenite grain boundary in the as-cladded sample (Figure 25a). After the tempering, massive nano precipitates are dispersed in the matrix of NMS (Figure 25b). When treated at 550 ℃ for 100 h, the precipitated particles became less but bigger (Figure 25c). This means that Ostwald ripening occurs in the alloy during this process. Small particles dissolve while large particles grow. Increasing the softening temperature to 600 ℃, this coarsening phenomenon is more distinct as shown in Figure 25d. These precipitates are expected to be C14-Laves phase by ThermoCalc simulation. Based on this, the lattice structure of the precipitates has been identified as hexagonal with lattice parameters of a = 0.468 nm and c = 0.764 nm. The determined lattice parameters are consistent with that of C14-Laves phase in literature [106]. Furthermore, the interface between C14-Laves phase and α-matrix is coherent (Figure 26). The mismatch between $d_{(10\bar{1}0)L}$ and $2d_{(110)\alpha}$ is as small as 1.9 %, resulting in low interfacial energy and consequently a consequently low driving force for the growth of the precipitates.

The hardness of NMS was significantly increased from ~ 380 HV to ~ 700 HV after being tempered, attributed to the massive precipitation of C-14 Laves phase in the steel and the absence of retained austenite, as shown in Figure 27. When exposed to elevated temperatures, the hardness decreases as expected. With respect to the tempered condition, the hardness drop is about 95 HV (to 605 HV) at 550 °C for 100 h and about 151 HV (to 531 HV) at 600 °C for 100 h. Compared to widely used H13 hot tool steel, NMS shows a much higher softening resistance and has a higher final hardness at the same conditions [107]. The good softening resistance of NMS at high temperatures is attributed to the low coarsening rate of the C-14 Laves phase. Two factors are responsible for this: the coherent interface with a small mismatch between Laves phase and the matrix, and the low diffusion coefficient of the controlling element (Mo).

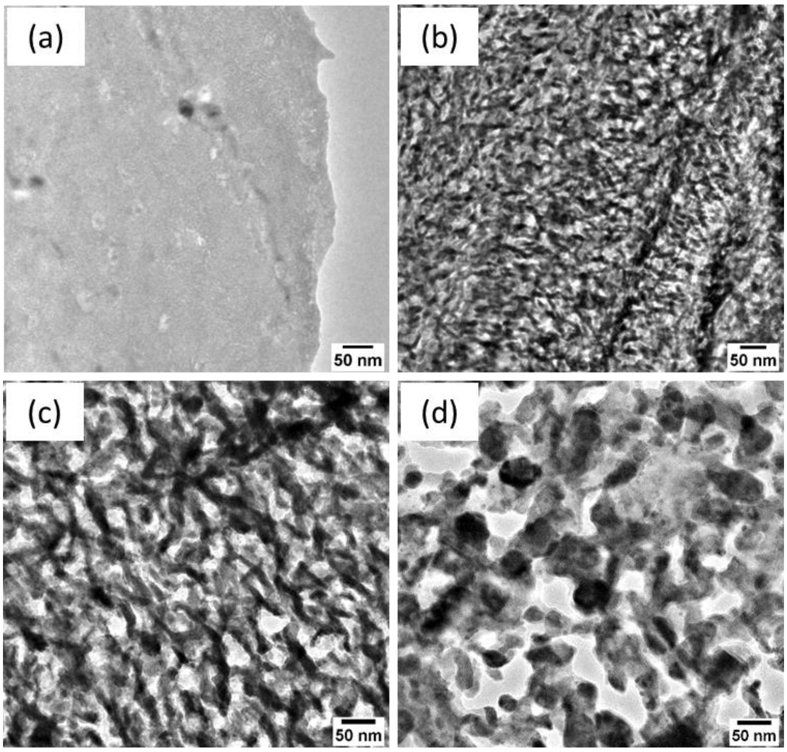
(a)
50 nm
(b)
50 nm
(c)
50 nm
(d)
50 nm

Figure 25. The evolution of the precipitates in NMS: (a) As-deposited; (b) Tempered; (c) Softened at 550 ℃ for 100 h; (d) Softened at 600 ℃ for 100 h.

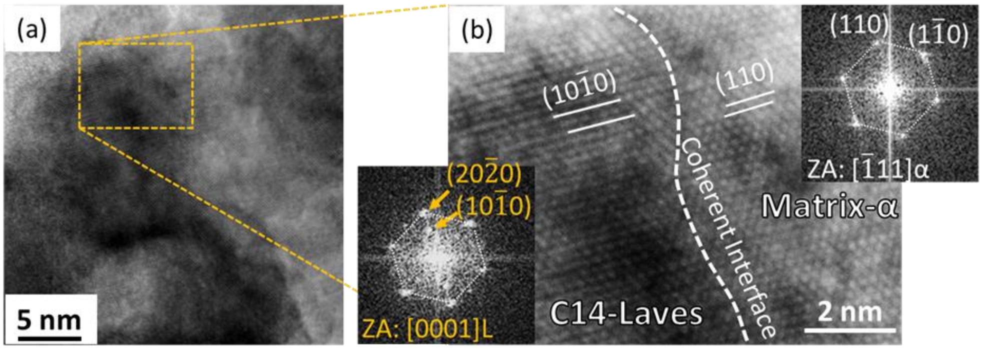
(a)
5 nm
(b)
$(10\bar{1}0)$
(110)
(110)
$(1\bar{1}0)$
ZA: $[\bar{1}11]\alpha$
Matrix-α
Coherent Interface
$(20\bar{2}0)$
$(10\bar{1}0)$
ZA: [0001]L
C14-Laves
2 nm

Figure 26. (a) High-resolution TEM image from the NMS alloy treated at 550 ℃ for 100 h ; (b) magnified image showing the lattice of the precipitate and the matrix. FFT patterns were obtained from different areas.

The coarsening behavior of the precipitates as a function of time and temperature is simulated by the revised LSW model (Equation 12 & 14), which is successful in general, as shown in Figure 28a. The simulated particle size agrees well with the experimental observation at 550 °C, while it is slightly larger than the measured one at 600 °C.

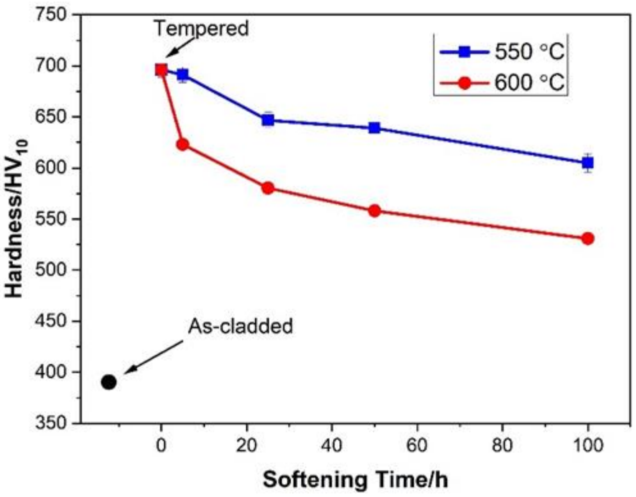

Figure 27. The hardness evolution of NMS after being treated at various conditions.

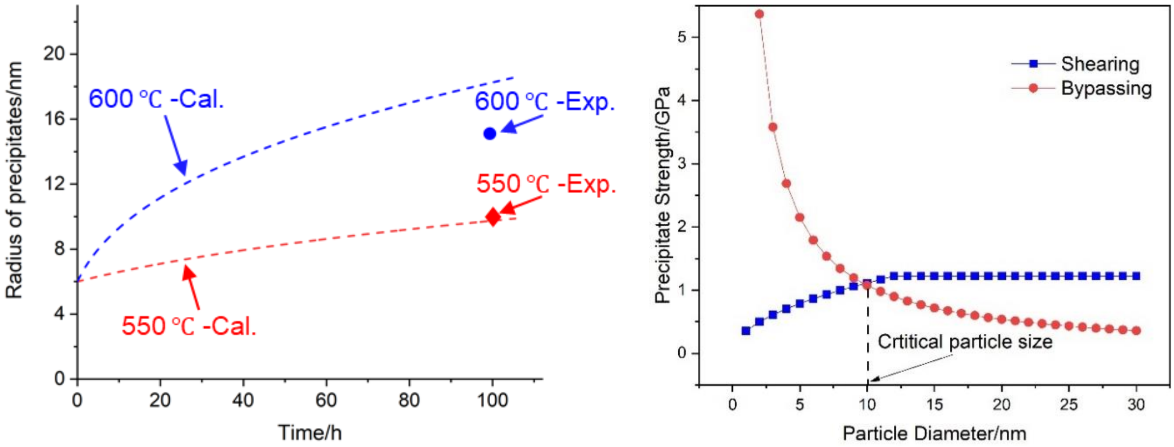

Figure 28. (a) Coarsening of the precipitates in NMS calculated by revised LSW model. (b) Precipitate strengthening effect as a function of particle diameter using the shearing and bypassing model.

Considering the double tempering (535 °C for 3 h) performed in this study, it is expected that the contribution of the dislocations to the strength is similar under different softening conditions. Since the fraction of precipitates is maintained at a constant level (~ 17 vol%) and the grain size does not grow up significantly, the influence of grain boundary and solid solution on the strength is less important in this case. Precipitate strengthening due to the interaction between dislocation and precipitate is the main strengthening mechanism in the current maraging steel. Two well-known models, the shearing and Orowan looping model (Equation (9), (10) and (11)), are used to describe the precipitation hardening, as shown in Figure 28b. The critical particle size determined is 10 nm. It is smaller than the average particle size in tempered NMS (~12 nm), meaning that bypassing mechanism is dominant and the strengthening effect of precipitates in the softened sample should be calculated by Equation (10) and (11). The estimated hardness drop is consistent with the experimental observation at both 550 °C and 600 °C. The detailed discussions are presented in **Paper IV**.

The softening behaviors of HBS and V4E steel at elevated temperatures are presented in **Paper V**. Figure 29 shows the hardness evolution of HBS, V4E and the base material (Dievar tool steel). The tempered HBS alloy obtained a high hardness of 1065 HV. After being exposed at 550 °C for 100 h, the hardness is still as high as 906 HV. The reduction of the hardness is just about 159 HV. When increasing the softening temperature to 600 °C, the hardness dropped to 647 HV after 100 h, indicating a significantly higher reduction of 418 HV. As to the V4E steel, it had an overall lower hardness compared with HBS alloy under all conditions. However, its hardness reduction is 103 HV after softening at 550 °C for 100 h and 323 HV after softening at 600 for 100 h, which are significantly lower than that of HBS alloy under the same conditions. This indicates that V4E has a better softening resistance than HBS alloy.

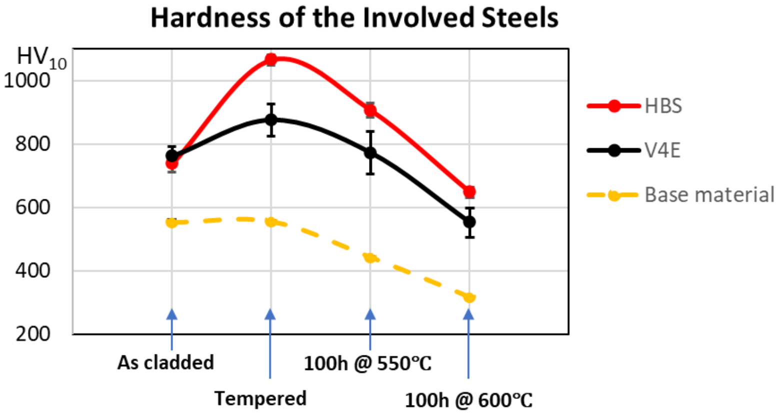

Figure 29. Hardens evolution of HBS and V4E at different states.

The microstructure evolution could interpret the large hardness drops of HBS during the softening. As can be seen in Figure 30a, with double tempering at 525 °C for 2 h, the matrix still reveals a relief-like structure, implying a high dislocation density in the tempered material, which provides dislocation hardening. Far more precipitates are found in Figure 30b after exposure at 550 for 100 h, implying a supersaturated solid solution in the tempered matrix. In a word, solid solution strengthening by alloying elements and dislocation hardening are important in the as-tempered condition. Although extensive precipitates occur in the 550 ℃ softened sample, the effect of solid solution strengthening and dislocation hardening weaken, the latter of which is indicated by the disappearance of the relief-like structure. The net effect is the decrease of final hardness, as exhibited in Figure 29. When increasing the softening temperature to 600 °C, the hardness of HBS alloy has a further decrease compared to that 550 °C. The coarsening of the precipitates (Figure 30c) and further lowered dislocation density are the reasons.

Compared to HBS alloy, V4E steel shows a better softening resistance (Figure 29). Notice the tempering temperature of V4E steel (550 ℃) is higher than that of HBS (525 ℃). This means the dislocations in V4E could be eliminated more during tempering and the density will not have a significant decrease during the subsequent softening. Another factor that may influence the softening resistance is the MC precipitates in V4E. V-enriched MC carbides are very hard and more stable than Cr-enriched $M_{23}C_6$ or M_7C_3 in HBS. This could be another reason that V4E shows a better softening resistance.

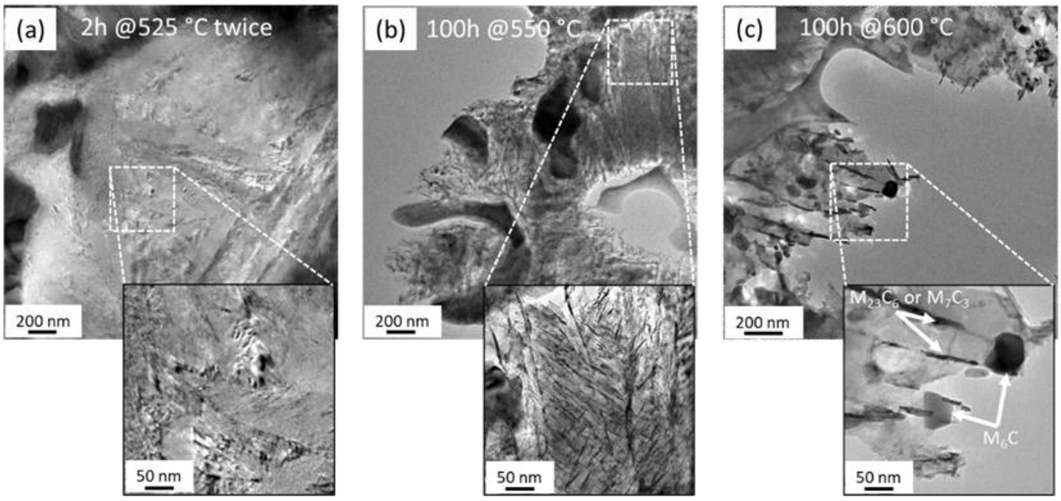

Figure 30. Transmission electron microscopy (TEM) of the HBS after (a) tempering, (b) softening at 550 °C and (c) 600 °C for 100 h.

7.3.3 Temperature Dependent Softening of Tool Steels Manufactured by DED

Since the tool steels could be subjected to temperatures as high as 800 ℃ during hot stamping processes, it is necessary to evaluate the softening resistance in a higher temperature regime. In Paper VI, the tempered tool steels are softened for 3 h at the high temperatures of 600, 700 and 800 ℃, respectively. Meanwhile, as a reference, the conventional counterparts are treated in the same way for comparison.

For HBS steel manufactured by DED, a typical microstructure in the tempered state includes the primary boride, eutectic region, and boride-free region. The further exposure at 600 for 3 h does not introduce microstructure change (Figure 31a). With the increase of softening temperatures, as shown in Figure 31b-c, fine precipitates became visible in the matrix at 700 ℃ and coarsened at 800 ℃. These precipitates are identified as M_6C carbides by XRD. $M_{23}C_6$ phase was also detected. The microstructure of softened V4E steel is shown in Figure 31d-f. In the tempered sample, a dendrite with eutectic structure and M_2C carbide located in the inter-dendritic region are formed. No detectable change can be found after subsequent exposure at 600 ℃. Some fine bright precipitates are observed in the inter-dendritic region at 700 ℃ and are dramatically coarsened at 800 ℃. Another type of dark precipitate as marked by arrows in Figure 31f can be seen in the matrix. These precipitates are probably newly precipitated MC carbide enriched in V. For AM-produced NMS, the as-tempered structure is mainly tempered martensitic with extremely fine precipitates which is difficult to be resolved by SEM. The precipitates are identified as C14-Laves phase (**Paper IV**). Similar to the other two steels, no change can be found at 600 ℃ compared to the tempered one (Figure 31g). However, with increasing softening temperature, these precipitates are coarsened (Figure 31h-i). Moreover, some particles have abnormal growth. Still, these precipitates show a fine size and uniform distribution in general.

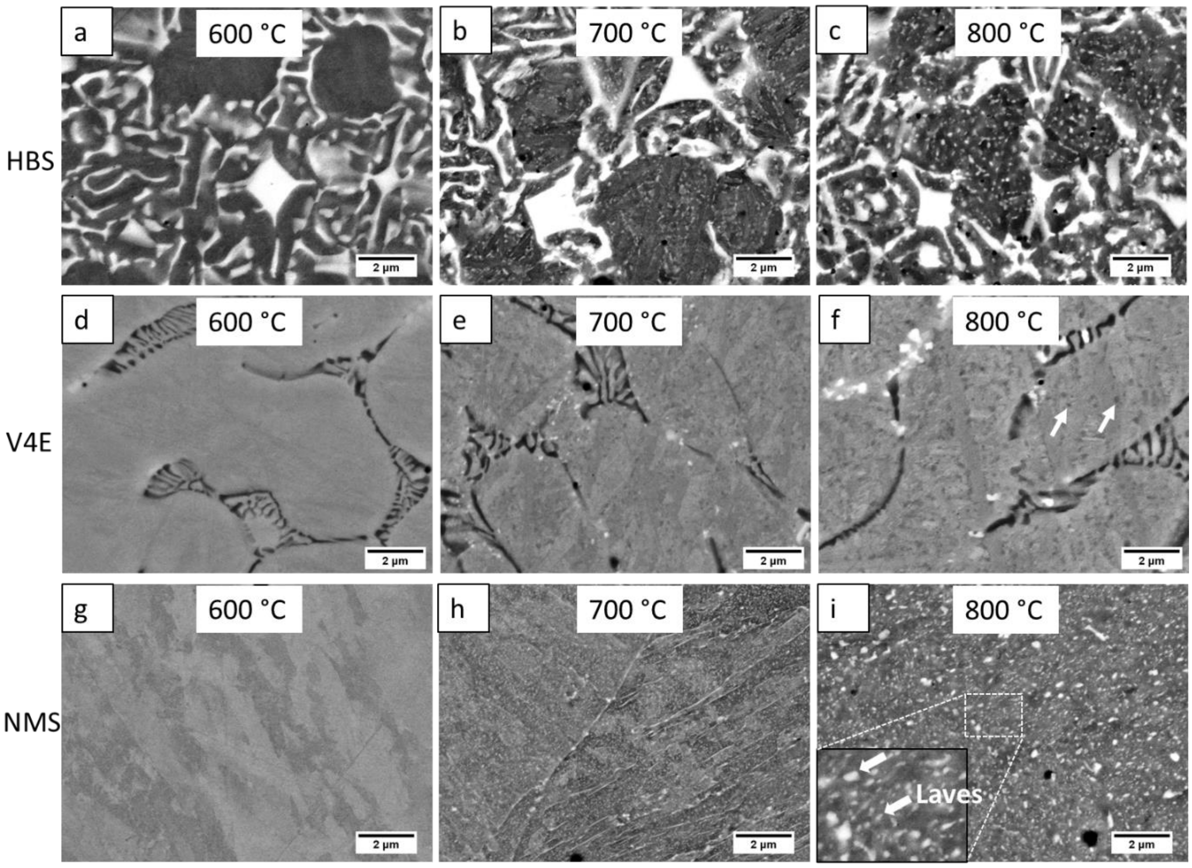

Figure 31. SE-SEM images of DEDed HBS (1st row), V4E (2nd row) and NMS (3rd row) after being softened at different temperatures for 3 h: (a), (d) and (g) 600 ℃, (b), (e) and (h) 700 ℃, (c), (f) and (i) 800 ℃. The white arrows mark MC carbide in (f) and Laves particles in (i).

Figure 32 shows the hardness variation of the AM-produced steels and conventional counterparts as a function of temperature. All three types of steels show a decreasing tendency with the increase in softening temperatures. A dramatic drop is found at 700 ℃, indicating the performance becomes worse when temperatures is above 700 ℃. The ranking of the overall hardness for these three types of steels in the tempered and softened condition is HBS > V4E > NMS up to ~ 640 ℃. At higher temperatures, the slower softening rate of NMS makes its hardness higher than that of V4E. For HBS and V4E, the conventional material has in general a lower hardness than its AM counterpart, while similar hardness is obtained for AM and conventionally manufactured NMS.

When considering the hardness drop with respect to the as-tempered condition, NMS alloy shows the best softening resistance among the studied steels. The reason for this is the low coarsening rate of the strengthening Laves phase due to the low diffusion coefficient of the controlling element (Mo) and low interfacial energy with the surrounding matrix, as discussed in Paper IV. The AM-produced and conventional NMS have almost the same softening behavior owing to the similar microstructure at different temperatures. For HBS alloy, AM-produced samples show a better softening resistance than the HIPed ones. This could be explained by the fast-cooling rate in additive manufacturing, which will lead to more alloying elements trapped in the matrix during the solidification. At elevated temperatures, some alloying elements could combine with carbon and form carbides contributing to precipitate strengthening in the matrix. For V4E steel, the AM-produced sample shows a better softening resistance at 600 °C than the conventional one. However, this advantage was significantly reduced at 700 °C and even disappeared at 800 °C. The possible reason for this is that the M_6C precipitates in AM-produced V4E are considerably coarsened (Figure 31f).

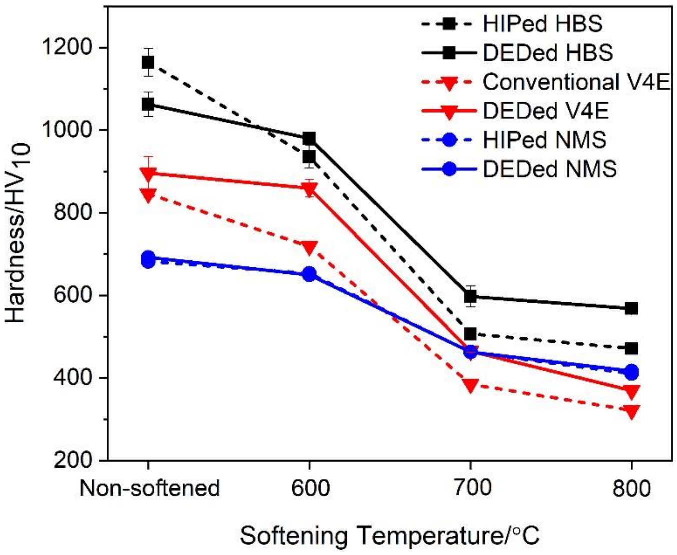

Figure 32. Hardness evolution of the AM-produced and conventional steels before and after being softened at different temperatures.

7.3.4 Wear Resistance

Due to the target application of hot stamping, wear resistance is of great importance. In the present study, the abrasive wear test has been carried out at room temperature after softening treatment. Weight reduction is used to evaluate their abrasive wear resistance, as shown in Figure 33. The ranking of the overall wear resistance at room temperature for three types of steels in the tempered and softened condition is HBS > V4E > NMS. The hardness ranking basically follows the same sequence until 640 °C. However, hardness is not the only factor that affects wear resistance. Conventional HBS and V4E have better wear resistance compared with AM counterparts despite lower hardness, while no difference is found for NMS.

NMS steel had the largest weight reduction of ~ 250 mg/min among these 3 types of steels, indicating a comparatively poor abrasive wear resistance. It is worth to mention that influence of temperature on weight reduction of NMS is insignificant and the values are relatively stable. In addition, there was basically no difference between the HIPed and AM samples in terms of weight reduction. These results echoed the similar microstructure evolution (Figure 31g-i and Figure 34g-i) and softening behavior (Figure 32) of HIPed and AM NMS. V4E steel presents a lower overall weight reduction than that of NMS steel (Figure 33), especially in the as-tempered condition, which is about 75 and 135 mg/min for conventional and AM samples, respectively. The weight reductions are increased with the softening temperature. Compared to the AM counterpart, the weight reductions of conventional V4E samples are lower except for the sample softened at 700 °C. This means that the conventional V4E steel has an overall better

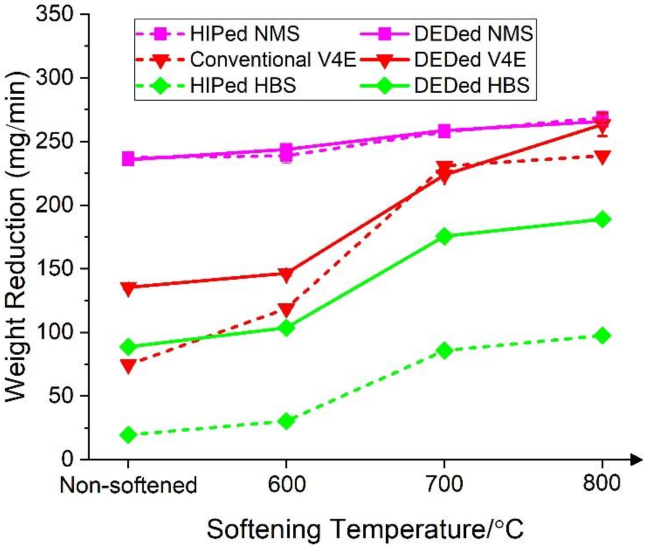

Figure 33. Weight reduction of the three steels before and after being softened at different temperatures.

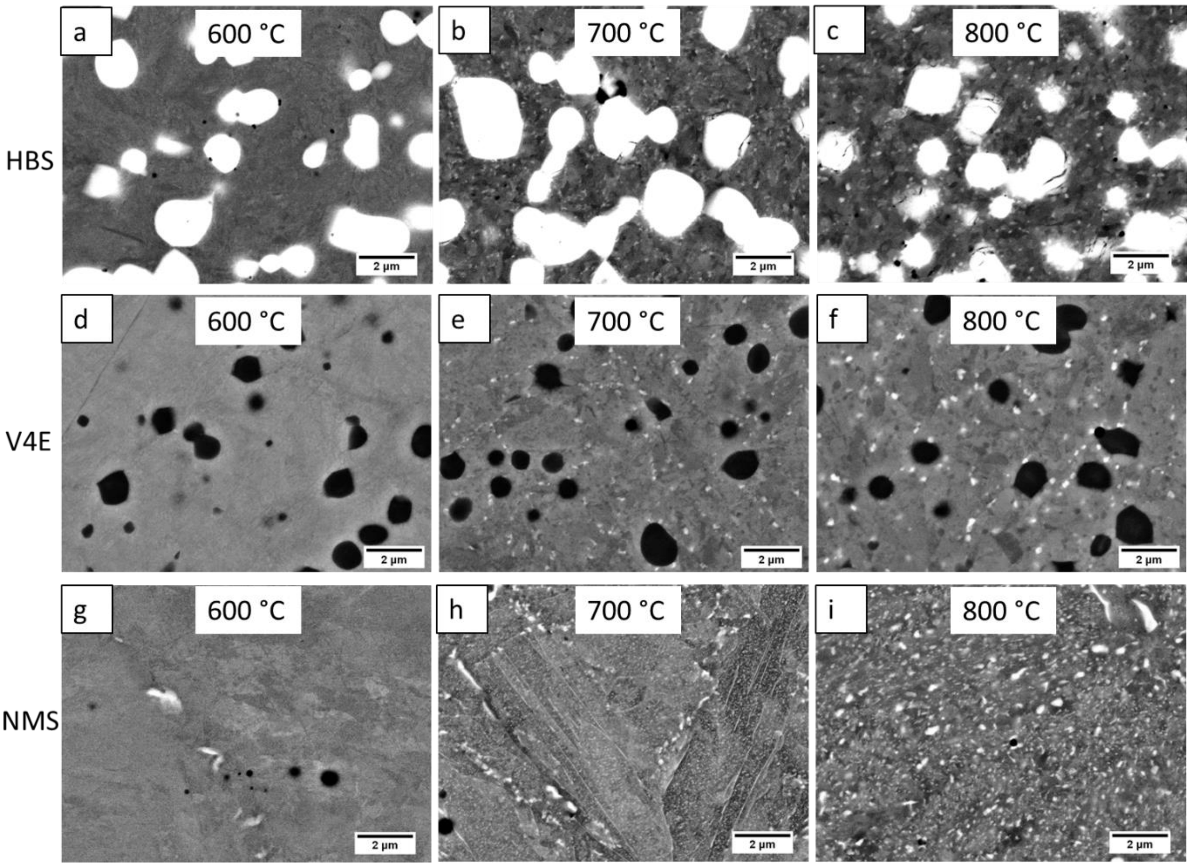
a
600 °C
b
700 °C
c
800 °C
HBS
d
600 °C
e
700 °C
f
800 °C
V4E
g
600 °C
h
700 °C
i
800 °C
NMS
2 μm

Figure 34. SE-SEM images of conventional samples of HBS (1st row), V4E (2nd row) and NMS (3rd row) after being softened at different temperatures for 3 h: (a), (d) and (g) 600 °C, (b), (e) and (h) 700 °C, (c), (f) and (i) 800 °C.

abrasive wear resistance than the AM counterpart, because the primary MC particle in conventional V4E steel has a larger average size than that in AM-produced samples, as shown in Figure 31d-f and Figure 34d-f. This phenomenon is further magnified in HBS steel. As can be seen in Figure 33, the HIPed HBS samples have extremely low weight reductions. The large difference on weight reduction between conventional and AM-produced HBS indicates that AM counterpart has a much worse wear resistance. The particle size of borides in conventional HBS (1.7 μm, Figure 34a-c) is much larger than that in conventional samples (0.4 μm, Figure 31a-c).

A hypothesis is proposed to explain this, as schematically shown in Figure 35. Coarse hard particles in the steels play an important role in the abrasive wear resistance. The average particle spacing (λ) and the average width (d_g) of the grooves influence the resistance to wear. λ can be estimated by using Equation (28) [76][108]:

$$\lambda = \frac{d_p}{2}\left(\sqrt{\frac{2\pi}{3f_v}} - 1\right) \tag{28}$$

where λ is the average diameter of particles, f_v is the volume fraction of the reinforcing phase. When the ratio $\lambda/d_g > 1$, the hard asperities from the sandpaper may scratch the matrix and plough away the matrix material easily, leading to reduce wear resistance. When the ratio $\lambda/d_g < 1$, on the contrary, the hard asperities cannot easily embed into the matrix and plough the materials, implying increased wear resistance. In this case, the hard asperities scratch the reinforcing particles instead of the matrix. For HIPed HBS, the estimated λ and d_g is about ~ 1.2 μm and ~ 1.5 μm, respectively. Therefore, $\lambda/d_g < 1$, meaning the HIPed HBS has outstanding abrasive wear resistance, as shown in Figure 35a. For conventional V4E (Figure 35b), λ (for MC carbides) is about 1.7 μm and dg is ~1.5 μm. Reasonable good abrasive wear resistance is obtained but worse than HBS. For NMS alloy (Figure 35c), due to the absence of hard particles with a size comparable to the asperities, it presents the worst abrasive wear resistance among three steels, and the resistance does not change much with its hardness.

More discussion can be found in **Paper VI**.

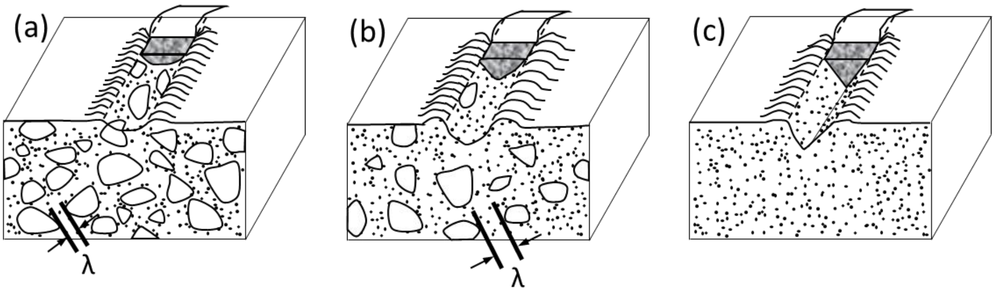

Figure 35. Schematic diagram of wear mechanisms in the three conventional steels: (a) HBS with small free spacing λ, (b) V4E with large free spacing λ among particles, (c) NMS. The small dots represent fine hard-phase particles in the matrix. The big particles represent the coarse hard-phase particles.

Chapter 8 – Conclusions

From the study in this thesis, the following conclusions can be drawn:

The case study performed on the hot stamping insert die showed that galling together with the spalling of the white layer are the primary wear mechanisms for the tool. Galling is a result of accumulated layers transferred from the steel workpieces to the die. Softening of the die material in the sublayer of ~ 200 μm promotes galling. The formation of the white layer is attributed to the repeated heating and quenching during hot stamping.

M-H13 hot work tool steel parts with high density were successfully fabricated by L-PBF method. The as-built samples have a fine cellular structure with a considerable amount of retained austenite. The effect of two types of post processing, direct tempering from as-built condition (DT) and conventional quenching followed by tempering (QT), on the microstructure and mechanical properties was evaluated. Despite of comparable tensile properties and hardness, DT samples exhibit significantly lower impact toughness compared to QT samples. This is attributed to the difference in work hardening ability and strain rate sensitivity. The DT samples have a better softening resistance at elevated temperatures than the QT samples, due to the smaller grain size of ferrite, less coarsened carbides and the cellular structure being preserved in DT samples.

Three different types of tool steels, Vanadias 4 Extralclean (V4E), a high-boron steel (HBS) and a newly developed martensitic steel (NMS), were cladded on a hot work tool steel by means of DED for hard-facing purpose. For all tool steels, a near-dense cladded zone was obtained except V4E. Defects, including pores and cracks, are formed in the deposited zone of V4E, the number of which increases with the building height or number of layers deposited. The formation of the large irregular pores is attributed to insufficient heat input and a thin Si oxide layer at the top of the internal surface. Hot cracking is related to several factors including the wide temperature range of solidification and the microstructure changes with the building height.

After being tempered, the cladded tool steels were exposed at elevated temperatures to assess the softening resistance. With the increase of temperature or time, the hardness decreases as expected. A large drop is found at 700 °C or above even for a relatively short dwell time of 3 h. HBS alloy has the highest overall hardness but the worst softening resistance, which is attributed to the drop of dislocation density and the coarsening of precipitates. The ranking of the overall hardness for three types of steels in the tempered and softened condition is HBS > V4E > NMS up to 700 °C for a short duration of 3 h. V4E steel has decent softening resistance. Stable secondary MC precipitates were considered as the key factor.

NMS has the lowest overall hardness but the best softening resistance among these three tool steels. The good softening resistance of NMS is attributed to the low coarsening rate of Laves phase due to a coherent interface with a small mismatch, and the low diffusion coefficient of the controlling element Mo. The coarsening behavior of the precipitates is simulated by the revised LSW model at 550 and 600 °C until 100 h. The simulation results agree well with the experimental observation. The hardness drops due to precipitate coarsening during high temperature exposure is also quantitatively analyzed using the precipitate strengthening models. The simulated hardness drop is consistent with the experimental observation at both 550 ℃ and 600 ℃.

The abrasive wear resistance of the steels manufactured by DED was evaluated after softening at 600, 700 and 800 °C for 3 h. The weight reductions are increased with the softening temperature. The ranking of the overall wear resistance at room temperature in the tempered and softened condition is HBS > V4E > NMS. Hardness is not the only factor that affects wear resistance. Conventional and AM-produced NMS have similar softening resistance and wear resistance in both tempered and softened conditions. This can be explained by the similar microstructure developed by these two manufacturing methods. Overall, AM HBS and V4E show better softening resistance but worse wear resistance compared with their conventional counterparts. Significantly different microstructures are found in these two conditions for HBS and V4E. The beneficial effect of AM on softening resistance is attributed to the stronger precipitation strengthening effect because of more secondary precipitates ($M_{23}C_7$ and/or M_6C for AM HBS, and MC for V4E). For abrasive wear resistance, the governing factor is supposed to be the ratio of λ/d_g (λ: free spacing between hard particles, d_g: average groove width). The narrow free spacing (λ) between coarse hard particles makes $\lambda/d_g < 1$, meaning outstanding abrasive wear resistance. This explains the better wear resistance for conventional HBS and V4E. The worst abrasive wear resistance of NMS is due to the absence of coarse hard particles.

Chapter 9 – Future Work

Based on the research presented in this thesis, some further work is suggested and summarized as followed:

(1) Optimization of process parameters. Considerable defects have been observed in the as-built V4E steel in this study. The optimization of process parameters to reduce defects for the DED V4E is needed. Hot cracking, which is caused by thermal stress, could be suppressed by increasing the preheating temperature of the base plate. Regarding porosity in DED V4E, slightly increasing the energy density may be helpful, because it can increase the wettability of liquid and give more time to pores to float up.

(2) High temperature wear test. The target application of the investigated tool steels is hot stamping. Hence, high temperature wear test is critical for the cladded samples. Currently, this test is still ongoing. There are still a lot of challenges, e.g., how to avoid heavy oxidation on both workpiece and tool steel, how to minimize the softening of tool steel samples during the tests and how to evaluate the galling and wearing behavior.

(3) Thermal fatigue test. Thermal fatigue is unavoidable in hot stamping processes. Designing a thermal fatigue test for cladded tool steels will be extremely useful to guarantee the safe use of the tools. Crack length and depth can be used to evaluate the thermal fatigue resistance.

(4) Dislocation density measurements. Dislocation density has a big influence on the strength of the materials, especially when the material is exposed to high temperatures. Quantification may make the prediction of mechanical properties of metals more reliable.

(5) Quantitative analysis of multi-precipitates strengthening mechanism. In Paper IV, the strengthening mechanism by a single type of precipitate has been discussed. In many situations, the strength of materials is governed by multi-precipitates. Quantitative analysis of this strengthening mechanism can more precisely describe the relationship between microstructure and properties.

Acknowledgements

First, I would like to thank my supervisor Prof. Yu Cao, examiner Prof. Lars Nyborg and co-supervisor Libin Liu for giving me the opportunity to take part in this interesting project and their valuable guidance and help during this special time.

I would also like to thank Uddeholms AB (Sweden) and ASSAB Tooling Technology (China) for providing support under which projects have been conducted. Special thanks go to Dr. Seshendra Karamchedu for his collaboration in terms of planning, guidance and providing the materials that were needed in this research. Christos Oikonomou, who takes over this project at the second stage, have done an excellent job! Many thanks to you! Also give thanks to Dimitrios Katsanos helping me with the tribological test and wonderful coffee time! In addition, I would like to thank Petter Damm and Aydin Selte from Uddeholms AB Sweden, Eason Fan and Wei Lun from ASSAB Tooling Technology China, Ye WeiJiang Jason, Voestalpine High Performance Metals Singapore, for their feedback during monthly work meetings.

Furthermore, I would like to acknowledge the research engineers Dr. Yiming Yao, who help me with TEM experiments, Dr. Eric Tam, Håkan Millqvist and Roger Sagdahl for their support in terms of practical work in this research.

Many thanks to the colleagues at Department of Industrial and Materials Science, for their supporting and encouraging for me to make the day in Sweden more enjoyable!

Finally, I would like to thank my family for their love, support and help even from the really long distance.

References

[1]. P. Kattire, S. Paul, R. Singh, and W. Yan, “Experimental characterization of laser cladding of CPM 9V on H13 tool steel for die repair applications,” J. Manuf. Process., vol. 20, pp. 492–499, 2015.

[2]. J. J. Yan et al., “Selective laser melting of H13: microstructure and residual stress,” J. Mater. Sci., vol. 52, no. 20, pp. 12476–12485, 2017.

[3]. T. Roy et al., “Effect of deposition material and heat treatment on wear and rolling contact fatigue of laser cladded rails,” Wear, vol. 412–413, no. May, pp. 69–81, 2018.

[4]. M. Åsberg, G. Fredriksson, S. Hatami, W. Fredriksson, and P. Krakhmalev, “Influence of post treatment on microstructure, porosity and mechanical properties of additive manufactured H13 tool steel,” Mater. Sci. Eng. A, vol. 742, no. August 2018, pp. 584–589, 2019.

[5]. K. Kempen, B. Vrancken, S. Buls, L. Thijs, J. Van Humbeeck, and J. P. Kruth, “Selective Laser Melting of Crack-Free High Density M2 High Speed Steel Parts by Baseplate Preheating,” J. Manuf. Sci. E-T ASME, vol. 136, no. 6, pp. 061026, 2014.R. Mertens, B. Vrancken, N. Holmstock, Y. Kinds, J. P. Kruth, and J. Van Humbeeck, “Influence of powder bed preheating on microstructure and mechanical properties of H13 tool steel SLM parts,” Phys. Procedia, vol. 83, pp. 882–890, 2016.

[6]. L. Xue, “Laser consolidation: A rapid manufacturing process for making net-shape functional components,” Adv. Laser Mater. Process. Woodhead Publishing, pp. 492–534, 2010.

[7]. J. Lee et al., “Microstructural effects on the tensile and fracture behavior of selective laser melted H13 tool steel under varying conditions,” Materials Characterization, vol. 155, pp. 109817, 2019.

[8]. S. Kou, “Welding metallurgy”. New Jersey, USA, pp.431-446, 2003.

[9]. S. Giganto, P. Zapico, M. Á. Castro-Sastre, S. Martínez-Pellitero, P. Leo, and P. Perulli, “Influence of the scanning strategy parameters upon the quality of the SLM parts,” Procedia Manuf., vol. 41, pp. 698–705, 2019.

[10]. R. Mertens, B. Vrancken, N. Holmstock, Y. Kinds, J. P. Kruth, and J. Van Humbeeck, “Influence of powder bed preheating on microstructure and mechanical properties of H13 tool steel SLM parts,” Phys. Procedia, vol. 83, pp. 882–890, 2016.

[11]. British standard BS EN ISO 4957:2000, Tool Steels; British Standards Institution, European Standard EN ISO 4957:1999E (English version). Tool Steels; European Committee for Standardization: Brussels.

[12]. L.S. Figiel, “On Damascus Steel,” Atlantis Arts Press, 1991.

[13]. J.M. Yumoto, “The Samurai Sword,” Charles E. Tuttle Company: Tokyo, Japan, 1958.

[14]. A. S. Townsend, “Alloy Tool Steels and the Development of High-Speed Steel,” Trans. Am. Soc. Steel Treat, Vol. 21, pp. 769-795, 1933.

[15]. Uddeholm, “Vanadis 4 Extra SuperClean,” pp. 1–8, 2016.

[16]. J. O. Milewski, “Additive manufacturing of metals,” Appl. Mech. Mater., 2017.

[17]. M. Jamshidinia, A. Sadek, W. Wang, S. Kelly. “Additive manufacturing of steel alloys using laser powder-bed fusion,” Adv. Mater. Process, vol. 173(1), pp. 20–24, 2015.

[18]. C. Kamath, B. El-dasher, G.F. Gallegos, W.E. King, A. Sisto, “Density of additively-manufactured, 316L SS parts using laser powder-bed fusion at powers up to 400 W,” Int. J. Adv. Manuf. Technol., vol. 74, pp. 65–78, 2014.

[19]. S. A. Khairallah, A. T. Anderson, A. M. Rubenchik, and W. E. King, “Laser powder-bed fusion additive manufacturing: Physics of complex melt flow and formation mechanisms of pores, spatter, and denudation zones,” Acta Mater., pp. 613–628, 2017.

[20]. T.M. Mower, M.J. Long, “Mechanical behavior of additive manufactured, powder-bed laser-fused materials”. Mater. Sci. Eng. A, vol. 651, pp.198–213, 2016.

[21]. A. Kudzal, B. McWilliams, C. Hofmeister, F. Kellogg, J. Yu, J. Taggart-Scarff, J. Liang, “Effect of scan pattern on the microstructure and mechanical properties of Powder Bed Fusion additive manufactured 17-4 stainless steel”, Mater. Des., vol. 133, pp. 205–215, 2017.

[22]. S. E. Brika, M. Letenneur, C. A. Dion, and V. Brailovski, “Influence of particle morphology and size distribution on the powder flowability and laser powder bed fusion manufacturability of Ti-6Al-4V alloy,” Addit. Manuf., vol. 31, no. August 2019, pp. 100929, 2020.

[23]. K. Riener et al., “Influence of particle size distribution and morphology on the properties of the powder feedstock as well as of AlSi10Mg parts produced by laser powder bed fusion (LB-PBF),” Addit. Manuf., vol. 34, no. April, pp. 101286, 2020.

[24]. X. Zhao, J. Chen, X. Lin, and W. Huang, “Study on microstructure and mechanical properties of laser rapid forming Inconel 718,” Mater. Sci. Eng. A, vol. 478, no. 1–2, pp. 119–124, 2008.

[25]. A. B. Spierings, N. Herres, and G. Levy, “Influence of the particle size distribution on surface quality and mechanical properties in AM steel parts,” Rapid Prototyp. J., vol. 17, no. 3, pp. 195–202, 2011.

[26]. K. Abd-Elghany and D. L. Bourell, “Property evaluation of 304L stainless steel fabricated by selective laser melting,” Rapid Prototyp. J., vol. 18, no. 5, pp. 420–428, 2012.

[27]. A. J. Pinkerton and L. Li, “Direct additive laser manufacturing using gas- and water-atomised H13 tool steel powders,” Int. J. Adv. Manuf. Technol., vol. 25, no. 5–6, pp. 471–479, 2005.

[28]. T. Fiegl, M. Franke, A. Raza, E. Hryha, and C. Koerner, "Effect of AlSi10Mg0. 4 long-term reused powder in PBF-LB/M on the mechanical properties." Mater. Design, vol. 212, pp: 110176, 2021.

[29]. D. Svetlizky, M. Das, B. Zheng, et al., "Directed energy deposition (DED) additive manufacturing: Physical characteristics, defects, challenges and applications." Mater. Today, vol. 49, pp: 271-295, 2021.

[30]. T. DebRoy, et al., "Additive manufacturing of metallic components–process, structure and properties." Prog. Mater. Sci., vol. 92, pp: 112-224, 2018.

[31]. E. Bojestig, Y. Cao, and L. Nyborg, “Surface chemical analysis of copper powder used in additive manufacturing,” Surf. Interface Anal., vol. 52, no. 12, pp. 1104–1110, 2020.

[32]. Y. Cao, M. Delin, F. Kullenberg, and L. Nyborg, “Surface modification of Ti-6Al-4V powder during recycling in EBM process,” Surf. Interface Anal., vol. 52, no. 12, pp. 1066–1070, 2020.

[33]. X. He, J. T. Norris, P. W. Fuerschbach, T. DebRoy, “Liquid metal expulsion during laser spot welding of 304 stainless steel,” J. Phys. D. Appl. Phys., vol. 39, no. 3, pp. 525–534, 2006.

[34]. K. A. Mumtaz, N. Hopkinson, “Selective laser melting of thin wall parts using pulse shaping,” J. Mater. Process Technol., vol. 210, no. 3, pp. 279-287, 2010.

[35]. T. Debroy et al., “Progress in Materials Science Additive manufacturing of metallic components – Process , structure and properties,” Prog. Mater. Sci., vol. 92, pp. 112–224, 2018.

[36]. M. Letenneur, A. Kreitcberg, and V. Brailovski, “Optimization of laser powder bed fusion processing using a combination of melt pool modeling and design of experiment approaches: Density control,” J. Manuf. Mater. Process., vol. 3, no. 1, 2019.

[37]. I. Yadroitsev, I. Yadroitsava, P. Bertrand, and I. Smurov, “Factor analysis of selective laser melting process parameters and geometrical characteristics of synthesized single tracks,” Rapid Prototyp. J., vol. 18, no. 3, pp. 201–208, 2012.

[38]. N. T. Aboulkhair, N. M. Everitt, I. Ashcroft, and C. Tuck, “Reducing porosity in AlSi10Mg parts processed by selective laser melting,” Addit. Manuf., vol. 1, pp. 77–86, 2014.

[39]. O. Hildreth, A. Nassar, K. Chasse, and T. Simpson, “Dissolvable metal supports for 3D direct metal printing,” 3d Print Addit. Manuf., vol. 3, nr. 2, pp. 90-97, 2016.

[40]. A. Mertens, S. Reginster, Q. Contrepois, T. Dormal, O. Lemaire, and J. Lecomte-Beckers, “Microstructures and mechanical properties of stainless steel AISI 316L processed by selective laser melting,” Mater. Sci. Forum, vol. 783–786, pp. 898–903, 2014.

[41]. K. Chadha, Y. Tian, K. Nyamuchiwa, et al., "Austenite transformation during deformation of additively manufactured H13 tool steel", Mater. Today Commun., vol. 33, pp: 104332, 2022.

[42]. M. Mazur, P. Brincat, M. Leary, M. Brandt, “Numerical and experimental evaluation of a conformally cooled H13 steel injection mould manufactured with selective laser melting,” Int. J. Adv. Manuf. Technol., vol. 93, pp. 881–900, 2017.

[43]. R. Mertens, B. Vrancken, N. Holmstock, Y. Kinds, J. P. Kruth, and J. Van Humbeeck, “Influence of powder bed preheating on microstructure and mechanical properties of H13 tool steel SLM parts,” Phys. Procedia, vol. 83, pp. 882–890, 2016.

[44]. J. Šafka, M. Ackermann, L. Voleský, “Structural properties of H13 tool steel parts produced with use of selective laser melting technology,” J. Phys. Conf. Ser., vol. 709, 2016.

[45]. M. J. Holzweissig, A. Taube, F. Brenne, M. Schaper, and T. Niendorf, “Microstructural Characterization and Mechanical Performance of Hot Work Tool Steel Processed by Selective Laser Melting,” Metall. Mater. Trans. B Process Metall. Mater. Process. Sci., vol. 46, no. 2, pp. 545–549, 2015.

[46]. R. Dörfert, J. Zhang, B. Clausen, H. Freiße, J. Schumacher, and F. Vollertsen, “Comparison of the fatigue strength between additively and conventionally fabricated tool steel 1.2344,” Addit. Manuf., vol. 27. pp. 217–223, 2019.

[47]. L. Xue, J. Chen, and S. H. Wang, “Freeform Laser Consolidated H13 and CPM 9V Tool Steels,” Metallogr. Microstruct. Anal., vol. 2, no. 2. pp. 67–78, 2013.

[48]. J. Mazumder, A. Schifferer, and J. Choi, “Direct materials deposition: designed macro and microstructure,” Mater. Res. Innov., vol. 3, pp. 118–131, 1999.

[49]. J. Choi, Y. Chang, “Characteristics of laser aided direct metal/material deposition process for tool steel,” Int. J. Mach. Tool Manuf., vol. 45, no. 4-5, pp. 597–607, 2005.

[50]. A. J. Pinkerton and L. Li, “Direct additive laser manufacturing using gas- and water-atomised H13 tool steel powders,” Int. J. Adv. Manuf. Technol., vol. 25, no. 5–6, pp. 471–479, 2005.

[51]. J. S. Park, J. H. Park, M. G. Lee, J. H. Sung, K. J. Cha, and D. H. Kim, “Effect of Energy Input on the Characteristic of AISI H13 and D2 Tool Steels Deposited by a Directed Energy Deposition Process,” Metall. Mater. Trans. A Phys. Metall. Mater. Sci., vol. 47, no. 5, pp. 2529–2535, 2016.

[52]. H. Chandler, “Heat Treaters’s Guide: Practices and Procedures for Irons and Steels, 2nd ed.,” ASM International, Materials Park, pp. 561–563, 1995.

[53]. J. Boes, A. Röttger, C. Mutke, C. Escher, and W. Theisen, “Microstructure and mechanical properties of X65MoCrWV3-2 cold-work tool steel produced by selective laser melting,” Addit. Manuf., vol. 23, no. July, pp. 170–180, 2018.

[54]. Z. H. Liu, D. Q. Zhang, C. K. Chua, K. F. Leong, “Crystal structure analysis of M2 high speed steel parts produced by selective laser melting,” Mater. Char., vol. 84, pp. 72–80, 2013.

[55]. K. Kempen, B. Vrancken, S. Buls, L. Thijs, J. Van Humbeeck, J.-P. Kruth, “Selective laser melting of crack-free high density M2 high speed steel parts by baseplate preheating,” J. Manuf. Sci. Eng., Vol. 136, pp. 061026, 2014.

[56]. J. Saewe, C. Gayer, L. Jauer, J. Kunz, C. Broeckmann, and J. H. Schleifenbaum, “Feasibility investigation for laser powder bed fusion of high-speed steels,” Euro PM 2018 Congress and Exhibition. 2020.

[57]. A. B. Spierings, N. Herres, and G. Levy, “Influence of the particle size distribution on surface quality and mechanical properties in AM steel parts,” Rapid Prototyp. J., vol. 17, no. 3, pp. 195–202, 2011.

[58]. G. Casalino, S. L. Campanelli, N. Contuzzi, and A. D. Ludovico, “Experimental investigation and statistical optimisation of the selective laser melting process of a maraging steel,” Opt. Laser Technol., vol. 65, pp. 151–158, 2015.

[59]. T. Mukherjee, J. S. Zuback, A. De, T. DebRoy, “Printability of alloys for additive manufacturing”. Sci. Rep., vol. 6, no. 1, pp. 1-8, 2016.

[60]. R. C. Barclay, “Parameter optimization for controlling aluminum loss when laser depositing Ti-6Al-4V,” Missouri University of Science and Technology, 2013.

[61]. A. Bauereiß, T. Scharowsky, and C. Körner, “Defect generation and propagation mechanism during additive manufacturing by selective beam melting,” J. Mater. Process. Technol., vol. 214, no. 11. pp. 2522–2528, 2014.

[62]. R. Cunningham et al., “Keyhole threshold and morphology in laser melting revealed by ultrahigh-speed x-ray imaging,” Science, vol. 363, no. 6429. pp. 849–852, 2019.

[63]. L. Thijs, F. Verhaeghe, T. Craeghs, J. Van Humbeeck, and J. P. Kruth, “A study of the microstructural evolution during selective laser melting of Ti-6Al-4V,” Acta Mater., vol. 58, no. 9. pp. 3303–3312, 2010.

[64]. D. Herzog, V. Seyda, E. Wycisk, C. Emmelmann, “Additive manufacturing of metals,” Acta Mater. Vol. 117, pp. 371–392, 2016.

[65]. C. Zhao, N. D. Parab, X. Li, K. Fezzaa, W. Tan, A. D. Rollett, & T. Sun, “Critical instability at moving keyhole tip generates porosity in laser melting,” Science, vol. 370, no. 6520, pp. 1080–1086, 2020

[66]. J. W. Elmer, J. Vaja, H. D. Carlton, and R. Pong, “The effect of Ar and N2 shielding gas on laser weld porosity in steel, stainless steels, and nickel,” Weld. J., vol. 94, no. 10. pp. 313s-325s, 2015.

[67]. C. PAUZON, “Tailored process gases for laser powder bed fusion.” Chalmers University of Technology, 2021.

[68]. F. Carter Giles, Materials science & engineering, Materials Park, Ohio:ASM International, 1991, ISBN 9780871703996.

[69]. S. Kou, “A criterion for cracking during solidification,” Acta Mater., vol. 88. pp. 366–374, 2015.

[70]. J. Liu and S. Kou, “Effect of diffusion on susceptibility to cracking during solidification,” Acta Mater., vol. 100. pp. 359–368, 2015.

[71]. H. Hyer et al., “Composition-dependent solidification cracking of aluminum-silicon alloys during laser powder bed fusion,” Acta Mater., vol. 208, p. 116698, 2021.

[72]. P. Bajaj, A. Hariharan, A. Kini, P. Kürnsteiner, D. Raabe, and E. A. Jägle, “Steels in additive manufacturing: A review of their microstructure and properties,” Mater. Sci. Eng. A, vol. 772, no. November 2019, 2020.

[73]. F. Huber et al., “Laser beam melting and heat-treatment of 1.2343 (AISI H11) tool steel – microstructure and mechanical properties,” Mater. Sci. Eng. A, vol. 742, no. November 2018, pp. 109–115, 2019.

[74]. J. H. Martin, B. D. Yahata, J. M. Hundley, J. A. Mayer, T. A. Schaedler, and T. M. Pollock, “3D printing of high-strength aluminium alloys,” Nat. Publ. Gr., vol. 549, no. 7672, pp. 365–369, 2017.

[75]. Meyers, Marc André, and Krishan Kumar Chawla. Mechanical behavior of materials. Cambridge university press, 2008.

[76]. K. Li, L. Wei, B. An, B. Yu, and R. D. K. Misra, “Aging phenomenon in low lattice-misfit cobalt-free maraging steel: Microstructural evolution and strengthening behavior,” Mater. Sci. Eng. A, vol. 739, no. August 2018, pp. 445–454, 2019.

[77]. Z. Guo and W. Sha, “Quantification of precipitation hardening and evolution of precipitates,” Materials Transactions, vol. 43, no. 6, pp. 1273–1282, 2002.

[78]. Wagner, Carl. "Theory of precipitate change by redissolution." Z. Elektrochem 65 (1961): 581-591.

[79]. Lifshitz, Ilya M., and Vitaly V. Slyozov. "The kinetics of precipitation from supersaturated solid solutions." J. Phys. Chem. Solids, vol. 19, no. 1-2, pp: 35-50, 1961.

[80]. Guo, Z., and W. Sha. "Quanti cation of precipitation kinetics and age hardening of Fe–12Ni–6Mn alloy during overaging." Mater. Sci. Technol., vol. 18, no. 5, pp: 529-533, 2002.

[81]. H. Nitta, T. Yamamoto, R. Kanno, et al.,. "Diffusion of Molybdenum in α-Iron." Acta Mater., vol. 50, no. 6, pp: 4117-4125, 2002

[82]. https://www.matcalc.at/index.php/documentation/technical-papers

[83]. J.E. Bailey, and P. B. Hirsch. "The dislocation distribution, flow stress, and stored energy in cold-worked polycrystalline silver." Phil. Mag., vol. 5, no. 53, pp: 485-497, 1960.

[84]. T. Zhou, J. Faleskog, R. P. Babu, J. Odqvist, H. Yu, and P. Hedström, "Exploring the relationship between the microstructure and strength of fresh and tempered martensite in a maraging stainless steel Fe–15Cr–5Ni," Mater. Sci. Eng. A, vol. 745. pp. 420–428, 2019.

[85]. S. Li, K.B. Lau, D. Wuu, et al., "3D printing of ductile equiatomic Fe-Co alloy for soft magnetic applications." Addit. Manuf., vol. 47, pp: 102291, 2021.

[86]. N. Kamikawa, K. Sato, G. Miyamoto, et al. "Stress–strain behavior of ferrite and bainite with nano-precipitation in low carbon steels." Acta Mater., vol. 83, pp: 383-396, 2015.

[87]. J.S. Wang, M.D. Mulholland, G.B. Olson, D.N. Seidman, "Prediction of the yield strength of a secondary-hardening steel," Acta Mater., vol. 61, pp: 4939–4952, 2013.

[88]. E. Galindo-Nava, P. Rivera-Díaz-del-Castillo, A model for the microstructure behaviour and strength evolution in lath martensite, Acta Mater. 98 (2015) 81–93.

[89]. T. Zhou, J. Lu, and P. Hedström, "Mechanical Behavior of Fresh and Tempered Martensite in a CrMoV-Alloyed Steel Explained by Microstructural Evolution and Strength Modeling," Metall. Mater. Trans. A Phys. Metall. Mater. Sci., vol. 51, no. 10, pp. 5077–5087, 2020.

[90]. H.P. Jost, "Lubrication (Tribology) Education and Research A Report on the Present Position and Industry's Needs", H. M. Stationary Office, London (1966).

[91]. J.T. Burwell, and C.D. Strang, "On the empirical law of adhesive wear", J. Appl. Phys., vol. 23, no. 1, pp: 18-28, 1952.

[92]. Stachowiak, Gwidon W., and Andrew W. Batchelor. Engineering tribology. Butterworth-heinemann, 2013.

[93]. Barge, M., G. Kermouche, P. Gilles, and J. M. Bergheau. "Experimental and numerical study of the ploughing part of abrasive wear." Wear, vol. 255, no. 1-6, pp: 30-37, 2003.

[94]. B. Bhushan, "Adhesion and stiction: mechanisms, measurement techniques, and methods for reduction." J. Vac. Sci. Technol. B, vol. 21, no. 6, pp: 2262-2296, 2003.

[95]. J. Song, and D. J. Srolovitz, "Adhesion Effects in Material Transfer in Mechanical Contacts." Acta Mater., vol. 54, no.19, pp: 5305–12, 2006.

[96]. M. H. Staia, Y. Pérez-Delgado, C. Sanchez, A. Castro, E. Le Bourhis, and E. S. Puchi-Cabrera, “Hardness properties and high-temperature wear behavior of nitrided AISI D2 tool steel, prior and after PAPVD coating”, Wear, vol. 267, no. 9–10. pp. 1452–1461, 2009.

[97]. C. Xu, and W. Gao. "Pilling-Bedworth ratio for oxidation of alloys", Mater. Res. Innov., vol. 3, no. 4, pp: 231-235, 2000.

[98]. https://en.wikipedia.org/wiki/Pilling%E2%80%93Bedworth_ratio#:~:text=The%20Pilling%E2%80%93Bedworth%20ratio%20(P,which%20the%20oxide%20is%20created).

[99]. O. C. Wells, “Scanning Electron Microscopy,” Encyclopedia of Materials: Science and Technology, pp. 8265-8269, 2001.

[100]. A. E384-17, Standard Test Method for Microindentation Hardness of MAterials, West Conshohocken, PA: ASTM International, 2017.

[101]. Q. Tan, Y. Yin, F. Wang, et al., "Rationalization of brittleness and anisotropic mechanical properties of H13 steel fabricated by selective laser melting." Scripta Mater., vol. 214, pp: 114645, 2022.

[102]. M. Lin, X. Zhao, L. Han, et al., "Microstructural evolution and carbide precipitation in a heat-treated H13 hot work mold steel." Metallogr., vol. 5, no. 6, pp: 520-527, 2016.

[103]. T.V. Philip, T.J. McCaffrey, Ultrahigh strength steels, in: G.T. Murray (Ed.), Handb. Mater. Sel. Eng. Appl, CRC Press, New York, 1997, pp. 149–162.

[104]. J. Sjöström, Chromium Martensitic Hot-Work Tool Steels, PhD Diss, 2004.

[105]. E. Louvis, P. Fox, C.J. Sutcliffe, Selective laser melting of aluminium components, J. Mater. Process. Technol., vol. 211, pp. 275–84, 2011.

[106]. S. Zhang, H. Fang, M.E. Gramsma, et al., Autonomous Filling of Grain-Boundary Cavities during Creep Loading in Fe-Mo Alloys, Metall. Mater. Trans. A Phys. Metall. Mater. Sci., vol. 47, no. 10, pp. 4831–4844, 2016.

[107]. M. Wang, W. Li, Y. Wu, S. Li, C. Cai, S. Wen, Q. Wei, Y. Shi, F. Ye, Z. Chen, High-Temperature Properties and Microstructural Stability of the AISI H13 Hot- Work Tool Steel Processed by Selective Laser Melting, Metall. Mater. Trans. B, vol. 50, no. 1, pp. 531–542, 2019.

[108]. M. Keränen, “Effect of Welding Parameters of Plasma Transferred Arc Welding Method on Abrasive Wear Resistance of 12V Tool Steel Deposit.” p. 169, 2010.